

Revision 2

23 pressure-volume-temperature data, yielding the following thermoelastic parameters:
24 $K_{T0} = 111(1)$ GPa, $K'_{T0} = 4.1(1)$, $(\partial K_0/\partial T)_P = -0.008$ (5) GPa K⁻¹ and $\alpha_T = 4(1) \times 10^{-5}$
25 K⁻¹ + $2(3) \times 10^{-8}$ K⁻²T. A strain analysis shows that the compression along the three
26 principal stress directions is highly anisotropic with $\epsilon_1:\epsilon_2:\epsilon_3 = 1.98:2.43:1.00$.
27 Additionally, high-pressure structural refinements of room-temperature polyhedral
28 geometry, bond lengths and O3-O3-O3 angle were investigated to ~27 GPa at
29 ambient temperature. Pressure dependences of polyhedral volumes and distortion
30 indicate that the substitution of Al³⁺ for Si⁴⁺ significantly changes the compressional
31 behavior of the TO₄-tetrahedron in augite. Density calculations of this augite along a
32 subducting slab geotherm suggest that augite as well as other common clinopyroxenes
33 would promote slab stagnations at transition zone depths if they are metastably
34 preserved in significant quantities.

35 **Keywords:** pyroxenes, augite, high pressure and temperature, single-crystal X-ray
36 diffraction, subduction zone

37

38 Introduction

39 Pyroxenes are among the most important rock-forming minerals and are commonly
40 found in both igneous and metamorphic rocks. Oceanic lithosphere consists of about
41 40% pyroxenes and garnet (Frost, 2008). It was believed that pyroxenes transform
42 into denser majorite garnet while oceanic crust subducts into the mantle (Akaogi and
43 Akimoto, 1977). However, recent studies imply that this reaction is inhibited under
44 cold slab conditions, so pyroxenes may survive in deeper parts of the mantle than was

Revision 2

45 previously thought (Nishi et al., 2008; Nishi et al., 2013; Van Mierlo et al., 2013).
46 Surviving metastable pyroxenes might cause stagnations of some slabs at depths
47 along the 660 km discontinuity, due to their lower densities compared to garnet and
48 broader metastability range compared to the metastable olivine (Agrusta et al., 2014;
49 King et al., 2015; Nishi et al., 2013; Van Mierlo et al., 2013). Therefore, knowledge
50 of the properties of pyroxenes to transition zone pressures (≥ 25 GPa) is very
51 important in modeling the subduction zone environments.

52 Among the pyroxene group minerals, augite is the most common species and occurs
53 in basalts and gabbros, which are major components of the oceanic crust. Augite is
54 also commonly found in andesites, diorites, peridotites and pyroxenites. Augite is
55 monoclinic ($C2/c$ space group) and has relatively complex crystal chemistry.

56 Pyroxenes have a general formula of $M2M1T_2O_6$. In augite, $M1$ sites are usually filled
57 with Mg^{2+} , Fe^{2+} , Ti^{3+} and Al^{3+} , $M2$ are larger polyhedral sites that commonly
58 accommodate Ca^{2+} , Na^+ , Fe^{2+} , and Mg^{2+} , while T sites are occupied predominantly by
59 Si^{4+} , but typically contains some Al^{3+} (Clark et al., 1969). In contrast with augite,
60 diopside [$CaMgSi_2O_6$] and hedenbergite [$CaFeSi_2O_6$] are usually Al-free. Although
61 pyroxene minerals have been extensively investigated at high pressures with the
62 discovery of several new polymorphs (Dera et al., 2013a; Finkelstein et al., 2014;
63 Plonka et al., 2012; Zhang et al., 2012), studies of augite at high pressures and
64 temperatures have been limited. Augite is important to the petrology of subducted
65 slabs, therefore it seems urgent to fill the gap in understanding of the compressional
66 behavior of this mineral at simultaneous high pressures and temperatures. In this

Revision 2

67 study, single-crystal X-ray diffraction measurements of natural augite were conducted
68 at 0-26.65(2) GPa at ambient temperature and the crystal structures were refined. The
69 *P-V-T* relations were measured at pressure-temperature conditions to 24.35(2) GPa
70 and 700 K, and thermal equation of state was determined. We discussed the potential
71 effect of metastable augite on subducting slab dynamics in this report.

72

73 **Sample and method**

74 Natural augite samples were collected from the Damaping pyroxenite, Zhangjiakou,
75 Hebei Province, China. The crystals were colored light green, and their chemical was
76 estimated as $[(Ca_{0.89}Na_{0.05}Mg_{0.06})(Mg_{0.74}Fe_{0.11}Al_{0.14}Ti_{0.01})(Si_{1.88}Al_{0.12})O_{6.00}]$ based on
77 results of electron microprobe analysis (EMPA). Small chips (size 0.035×0.040 mm)
78 of single-crystal augite with thicknesses less than 0.010 mm were extracted from a
79 larger EMPA sample for this study. A single crystal was first mounted onto a polymer
80 micromesh sample holder (MiTeGen) for ambient-condition X-ray diffraction study.
81 One single crystal was used for each high pressure/temperature experiment. A BX90
82 DAC (Kantor et al., 2012) was used for high-pressure measurements at ambient
83 temperature. This DAC was equipped with two type-I diamond (300 μm culets)
84 mounted on Boehler-Almax-type WC seats, which had ±30 deg. opening angles. A
85 rhenium gasket was used and pre-indented to ~40 μm thickness before a laser drilling
86 of a 190-μm-diameter hole. The augite sample was loaded into the sample chamber
87 with Au powder serving as the pressure calibrant (Fei et al., 2007). At each pressure,
88 Au diffraction patterns were collected before and after sample data collection and the

Revision 2

89 average pressure values were used. A small ruby sphere of $\sim 10\ \mu\text{m}$ was also loaded
90 and used as the pressure indicator for the gas-loading with Ne as the
91 pressure-transmitting medium using the GSECARS gas-loading system (Rivers et al.,
92 2008). An externally heated DAC (EHDAC) was used for high-pressure and
93 high-temperature experiments. Temperatures up to 700 K were generated by
94 resistive-heating and measured with a K-type thermocouple attached to one of the
95 anvils $\sim 500\ \mu\text{m}$ away from the diamond culet. Likewise, Au powder, a ruby sphere
96 and a single-crystal sample were loaded, and Ne was used for pressure-transmitting
97 medium.

98 All of the X-ray diffraction experiments in this study were carried out at experimental
99 station 13-BM-C of the Advanced Photon Source, Argonne National Laboratory. The
100 incident X-ray beam was monochromated to a wavelength of $0.4340\ \text{\AA}$, and
101 collimated to a focal spot size of $15 \times 15\ \mu\text{m}^2$. Diffraction images were acquired on a
102 MAR165 CCD detector. Tilting and rotation of the detector and the
103 sample-to-detector distance were calibrated using ambient LaB_6 as the diffraction
104 standard. To obtain adequate number of diffraction for structure refinements, we
105 collected data at 4 different detector positions achieved by rotating the detector on the
106 6-circle goniometer. At D1 position the detector was perpendicular to the incident
107 X-ray direction, D2 was achieved by rotating the detector about the horizontal axis by
108 20° , whereas D3 and D4 were involved rotating about the vertical axis by 10° and
109 -10° , respectively. Wide and stepped φ exposures were collected for single-crystal
110 samples at each P - T point at D1 position, with an exposure time of $2\ \text{s}^\circ$. Wide

Revision 2

111 segment exposures with 10° rotation step were collected at each detector position. The
112 φ scan rotation axis was horizontal and perpendicular to the incident X-ray direction.
113 The ATREX/RSV software package (earlier known as GSE_ADA/RSV, (Dera et al.,
114 2013b)), was used to analyze the diffraction images. The lattice parameters and
115 orientation matrix were determined with the RSV software and the reduced reflection
116 data from the four detector positions were merged together. Unit-cell parameters at
117 each P - T condition are reported in Table 1. Crystal structures of augite at high
118 pressures were refined from the intensity data using SHELXL software via the Olex 2
119 user interface (Dolomanov et al., 2009; Sheldrick, 2007), starting from atomic
120 coordinates of Clark et al. (1969). According to the microprobe chemistry and
121 previously reported augite structure model (Clark et al., 1969), the site occupancies
122 were refined without vacancies. The $M2$ sites were fully occupied by Ca^{2+} , Mg^{2+} and
123 Na^+ , Fe^{2+} , Mg^{2+} , Ti^{3+} and Al^{3+} occupied the $M1$ sites, while the T sites contained Si^{4+}
124 and Al^{3+} . Cations in the same polyhedral site were set to share the same atomic
125 displacement parameters (ADPs) and the same fractional coordinates. The anisotropic
126 ADPs were only used for cations, due to the limited number of unique observations.
127 At ambient pressure the site-occupancy refinement for the $M2$, $M1$ and T sites led to a
128 mean electron number of 19.2, 13.4 and 14.0 which are very close to the numbers
129 calculated on the basis of the chemical data (19.1, 13.8 and 13.9 for $M2$, $M1$ and T
130 sites, respectively). The refined sum of mean electron number is also in general
131 agreement with the microprobe composition, so the cation contents based on the
132 EMPA composition were used in refinements. We also modeled the site distribution

Revision 2

133 of Fe between *M2* and *M1* sites, and the result indicated that the *M2* site is free of Fe.
134 Previous studies suggested that Fe³⁺ could be included in *M1* sites in addition to Fe²⁺,
135 based on Mössbauer measurements and other calculation methods, but only in small
136 quantities (Clark et al., 1969). Clark et al. (1969) proposed a method to infer the
137 Fe³⁺/Fe²⁺ distribution in augite based on the *M1*-O distance values. In this approach
138 *M1*-O distance in augite is assumed to be a simple linear combination of the average
139 *M1*-O distances observed in various end-member compositions. According to this
140 method and the use of the *M1*-O values of jadeite [NaAlSi₂O₆], diopside [CaMgSi₂O₆],
141 aegirine [NaFeSi₂O₆] (Clark et al., 1969), hedenbergite [CaFeSi₂O₆] (Zhang et al.,
142 1997) and [NaTiSi₂O₆] (Ullrich et al., 2010) combined with the *M1*-O value in this
143 study, we concluded that our augite sample is free of Fe³⁺. In high-pressure
144 refinements the site occupancy parameters of the cations were fixed based on the
145 EMPA and ambient-pressure structure refinement. Details of the structural
146 refinements, atomic coordinates, bond lengths and angles are reported in Tables 2, 3
147 and 4. Because of the limited opening angle ($\pm 17^\circ$) of the EHDAC, the structure
148 refinements were not possible.

149

150 **Results and discussion**

151 **Equation of state of augite at 298 K**

152 Figures 1 and 2 present the unit-cell parameters of augite as a function of pressure. *V*,
153 *a*, *b*, *c* and β angle undergo nonlinear decrease to 26.65(2) GPa with no discontinuity
154 in the compression curves. A third-order Birch–Murnaghan equation of state (BM3

Revision 2

155 EoS) was fit with the P - V data using the EosFit7c program (Angel et al., 2014). The
156 isothermal bulk modulus (K_{T0}) and its pressure derivative (K'_{T0}) were calculated to be
157 111(1) GPa and 4.1(2). The Eulerian finite strain ($f_E = [(V_0/V)^{2/3} - 1]/2$) versus
158 “normalized pressure” ($F_E = P/[3f_E(2f_E+1)^{5/2}]$) plot (Angel, 2000) was also used to
159 analyze the P - V data, and a weighted linear fit yielded an intercept value of 111(1)
160 GPa which is in good agreement with the results indicated by BM3 EoS (Figure 3).
161 The linear moduli of a , b and c were also calculated using the linear BM3 equation
162 (Figure 1) and EosFit7c program. The compressibilities (β) (Angel, 2000) of each axis
163 were calculated (Table 5) yielding $\beta_a:\beta_b:\beta_c=1:1.44:1.11$, which shows that b has the
164 highest compressibility and c is more compressible than a .

165

166 **Strain analysis**

167 Strain tensor analysis was performed to assess the degree of anisotropy between
168 principal stress directions, because the a - and c -axis are not the principal strain axes
169 while b -axis is coincident with one of them. Unit-cell parameters of augite were used
170 to analyze unit strain ellipsoid with win_STRAIN (Angel 2015), modified after
171 Ohashi (1982). Table 6 shows the strain values and directions of the three major
172 compression axes at each pressure. In order to visualize the orientation of the strain
173 tensor, we calculated the representation quadratic surface of augite using the method
174 suggested by Knight (2010). As shown in Figure 4, the softest major axis is parallel to
175 the b -axis, and the stiffest direction is oriented in the a - c plane.

176

Revision 2

177 **Polyhedral compression and distortion**

178 The evolutions of the volume of the $M2O_8$ -polyhedron, $M1O_6$ -octahedron and
179 TO_4 -tetrahedron with increasing pressure were investigated and shown in Figures 5
180 and 6. The eight coordinated $M2O_8$ -polyhedron is the most compressible while the
181 TO_4 -tetrahedron is the least. Likewise, the compression of the $M2O_8$ -polyhedron is
182 the smoothest, and the TO_4 -tetrahedron is the least smooth. The distortions of these
183 polyhedra were also analyzed (Robinson et al., 1971). As shown in Figure 7 the
184 distortion index of the $M2O_8$ -polyhedron decreases quickly with increasing pressure
185 up to ~ 15 GPa, where it becomes less responsive to pressure. This change can be
186 explained by examining evolutions of the bond lengths with pressure. As shown in
187 Figure 8 the longest bonds $M2-O3(C2, D2)$ becomes comparable to other bonds at
188 about 15 GPa. The $M1O_6$ -octahedron has the smallest distortion index, which
189 decreases to the minimum at ~ 20 GPa, and then increases again to a value comparable
190 to the ambient distortion (Figures 7 and 9).

191 Pyroxenes are characterized by single chains of tetrahedra that extend parallel to the
192 c -axis. These chains have significant rotation freedoms at high pressures, which can
193 be described by the reduction of the O3-O3-O3 angle (Figures 10 and 11). The \angle
194 O3-O3-O3 of augite shows a linear decrease of approximately $-0.47^\circ/\text{GPa}$ in the
195 pressure range of 0-8.30(4) GPa, then experiences a minor increase with increasing
196 pressure between 8.30(4) and 11.40(3) GPa (Table 4 and Figure 11). This is similar to
197 what was reported for kosmochlor $[\text{NaCrSi}_2\text{O}_6]$ (Posner et al., 2014), in which the
198 inflection occurs at 31.3 GPa. In augite this “hardening” of rotation of tetrahedral

Revision 2

199 chains is accompanied by a volume drop of TO_4 -tetrahedra in augite (Figure 6), which
200 was also observed in kosmochlor (Posner et al., 2014). Above 11.40(3) GPa the \angle
201 O3-O3-O3 decreases again, this time at an approximate rate of (0.37°/GPa), as the
202 TO_4 -tetrahedra become more incompressible (Figure 6). However, the
203 pressure-dependencies of the unit-cell volume and lattice parameters do not exhibit
204 any distinct discontinuities correlated with this curious behavior of the O3-O3-O3
205 angle (Figures 1 and 2).

206

207 **Thermal equation of state**

208 The unit-cell parameters of augite at various P - T conditions are given in Table 1, and
209 were used for subsequent calculations. Figure 12 shows the volume data measured at
210 298, 500 and 700 K. The high-temperature Birch-Murnaghan (HTBM) equation was
211 fit with the P - V - T data. The equation is given by the following form:

$$212 P = (3/2) K_{T0} [(V_{T0}/V)^{7/3} - (V_{T0}/V)^{5/3}] \times \{1 + (3/4)(K'_{T0} - 4)[(V_{T0}/V)^{2/3} - 1]\} \quad (1)$$

213 where K_{T0} , K'_{T0} and V_{T0} are bulk modulus, its pressure derivative and the unit cell
214 volume at ambient pressure and temperature (in Kelvin), respectively. The effects of
215 temperature on K_{T0} and V_{T0} are expressed by the follows:

$$216 V_{T0} = V_0 \exp \int_{300}^T \alpha_T dT \quad (2)$$

$$217 K_{T0} = K_0 + (\partial K_0 / \partial T)_P \times (T - 298) \quad (3)$$

$$218 \alpha_T = \alpha_0 + \alpha_1 T \quad (4)$$

219 where $(\partial K_0 / \partial T)_P$ and α_T are the temperature derivative of the bulk modulus and the
220 volumetric thermal expansion at ambient pressure.

Revision 2

221 Fitting the P - V - T data to the HTBM (1) yielded $K_{T0} = 111(1)$ GPa, $K_{T'0} = 4.1(1)$,
222 $(\partial K_0/\partial T)_P = -0.008$ (5) GPa K^{-1} and $\alpha_T(K^{-1}) = 4(1)\times 10^{-5} + 2(3)\times 10^{-8}T$. In view of the
223 relatively low temperature range (298-700 K in this study) and limited
224 high-temperature data, α_T is often assumed to be constant over the temperature range
225 i.e. $\alpha_T = \alpha_0$ (e.g., Nishihara et al., 2003; Xu et al., 2016). Therefore, the P - V - T data
226 were also fitted by constraining $\alpha_T = \alpha_0$, which yielded $K_{T0} = 111(1)$ GPa, $K_{T'0} =$
227 $4.1(1)$, $(\partial K_0/\partial T)_P = -0.008$ (5) GPa K^{-1} and $\alpha_T(K^{-1}) = 5.1(3)\times 10^{-5}$. The K_{T0} values
228 derived from high-temperature and pressure data are in excellent agreement with that
229 from EoS fit at ambient temperature ($K_{T0} = 111(1)$ GPa).

230

231 **Comparison with previous studies**

232 Due to the compositional complexity of augite, it is necessary to evaluate the effects
233 of cation substitutions on polyhedral compressions. Here we compared the polyhedral
234 compressions of augite and other important clinopyroxene end-members including
235 jadeite [$\text{NaAlSi}_2\text{O}_6$], diopside [$\text{CaMgSi}_2\text{O}_6$], hedenbergite [$\text{CaFe}^{2+}\text{Si}_2\text{O}_6$] and aegirine
236 [$\text{NaFe}^{3+}\text{Si}_2\text{O}_6$], all of which have $C2/c$ symmetry. In these pyroxenes the $M2$ site is
237 normally occupied by Ca^{2+} (eight coordinated) and Na^+ (six coordinated) (Downs,
238 2003), and the Ca^{2+} - and Na^+ -polyhedra exhibit about comparable compression below
239 ~ 8 GPa, above which the Ca^{2+} -polyhedra are more incompressible than Na -polyhedra.
240 Our augite has minor Na and Mg contents in addition to Ca^{2+} occupying the $M2$ Site,
241 but this substitution does not distinctly change the compression behavior of the
242 Ca^{2+} -dominated polyhedral, as shown in Figure 13(a). In comparison with the $M2$ site,

Revision 2

243 different cations occupying the *M1* site have distinct effects on the compression of the
244 *M1*-octahedron (Figure 13(b)). The *M1* site fully occupied by Al^{3+} is the most
245 incompressible among these clinopyroxenes, while the Mg-octahedron is the most
246 compressible. Fe^{2+} - and Fe^{3+} -octahedra have distinctly different compression trends,
247 with the latter being stiffer (McCarthy et al., 2008b), and comparable to the
248 Al^{3+} -octahedron, while Fe^{2+} is nearer to the Mg^{2+} -octahedron. The *M1* site of augite
249 in this study is mainly Mg^{2+} -occupied, but has significant contents of Fe^{2+} and Al^{3+} ,
250 and below ~ 11 GPa the compression of the octahedron is similar to that of
251 Mg^{2+} -octahedron in diopside. Above ~ 11 GPa, it becomes stiffer and closer to the
252 trend of the Fe^{2+} -octahedron in hedenbergite. The *T* site is almost fully filled by Si^{4+}
253 in most pyroxene minerals, but can contain small amount of Al^{3+} in augite (e.g., Bindi
254 et al., 2003; Hazen and Finger, 1977). In this study we investigated the effect of the
255 incorporation of Al^{3+} into the *T* site on the tetrahedral compression. As shown in
256 Figure 13(c), the Al-free end-member *C2/c* pyroxenes display very similar tetrahedral
257 compression trends, while the compression of the T-tetrahedron augite is notably
258 different, below ~ 13 GPa it also results in the compression trend, however, after that
259 it has a distinct volume drop at ~ 14 GPa as indicated by the pressure dependences of
260 the O3-O3-O3 angle and the *T*-O bond lengths (Figures 11 and 14). We also used a
261 second-order BM EOS to calculate the zero-pressure bulk modulus (K_{T0}) values of
262 these T-tetrahedra, and the results suggest that augite has a larger tetrahedral K_{T0}
263 (345(30) GPa) than aegirine (328(22) GPa), hedenbergite (306(16) GPa) and diopside
264 (321(15) GPa), but smaller than jadeite (386(10) GPa). Therefore, the tetrahedral K_{T0}

Revision 2

265 values of clinopyroxenes depend not only on cations occupying the *T* sites. To
266 summarize, the incorporation of Na⁺ and Mg²⁺ does not significantly change the
267 *M2*-polyhedral compression in augite. The substitutions of Fe²⁺ and Al³⁺ in the *M1*
268 site, however, cause a distinct *M1*-octahedral compression change after ~11 GPa. The
269 most significant effect of the cation substitution occurs in the *T* site, with an evident
270 tetrahedral volume drop during the compression.

271 The K_{T0} value of augite (whole crystal) obtained in this work was also compared with
272 previous investigations of jadeite, diopside, hedenbergite and aegirine. It is clear that
273 the polyhedral compression is not the only factor that constrains the K_{T0} values of
274 these pyroxenes. Among these C2/c pyroxenes jadeite has the most incompressible
275 *M1*-octahedron and the largest K_{T0} value that ranges from 124.5(4) to 136.5(14) GPa
276 (McCarthy et al., 2008a; Nestola et al., 2006; Posner et al., 2014; Zhao et al., 1997),
277 and hedenbergite [CaFe²⁺Si₂O₆] and aegirine [NaFe³⁺Si₂O₆] have nearly identical K_{T0}
278 values (116.1(5)-117(1) GPa) (Downs and Singh, 2006; McCarthy et al., 2008b;
279 Nestola et al., 2006; Zhang et al., 1997; Zhao et al., 1998), even though the
280 Fe²⁺-octahedron is much more compressible than the Fe³⁺-octahedron. Previous
281 studies on diopside give a relatively large range of K_{T0} values (104.1(9)-118(1) GPa)
282 (Aleksandrov and Ryzhova, 1961; Levien and Prewitt, 1981; Thompson and Downs,
283 2008; Zhang et al., 1997). In this study, the K_{T0} value (111(1) GPa) of a
284 diopside-dominant augite derived from a BM3 Eos fitting of the *P-V* data is also
285 within the value range of the pure diopside, although significant Al³⁺ and Fe²⁺ were
286 incorporated in the *M1* and *T* sites.

Revision 2

287 Numerous thermal expansion studies have been conducted on pyroxene minerals, and
288 the values of α_T show a large variation range ($1.84\text{-}9.26\times 10^{-5} \text{ K}^{-1}$) with various
289 compositions and structures (see summarizations in Yang and Prewitt (2000) and
290 Tribaudino and Mantovani (2014)). Augite in this study is diopside-rich and has a α_T
291 value of $5.1(3)\times 10^{-5} \text{ K}^{-1}$, which is higher than that of previous studies of diopside end
292 member $[\text{CaMgSi}_2\text{O}_6]$ ($3.41\text{-}3.44\times 10^{-5} \text{ K}^{-1}$) (Finger and Ohashi, 1976; Richet et al.,
293 1998). The discrepancy is likely due to the compositional difference. Augite in this
294 study has significant contents of Al in the *M1* and *T* sites, compared to the end
295 member-diopside. Incorporation of Al was previously regarded as a reason for
296 decrease in the thermal expansion (Tribaudino and Mantovani, 2014).

297

298 **Implications**

299 Clinopyroxenes are major components of Earth's upper mantle. The (Ca, Mg)-rich
300 clinopyroxenes provide important constraints when modeling the mineralogy of the
301 upper mantle (Frost, 2008). At normal mantle temperature condition clinopyroxenes
302 would disappear at transition zone depth because they are dissolved into majorite
303 garnet (Ringwood, 1982). However, clinopyroxenes could survive in subducting slabs
304 to greater depths because the pyroxene-garnet transition would be inhibited at
305 relatively low slab temperatures (Bina, 2013; Nishi et al., 2013; Van Mierlo et al.,
306 2013). On the other hand, high-pressure experimental studies demonstrate that
307 common Ca and Na-rich clinopyroxenes (with *C2/c* space group) like diopside
308 $[\text{CaMgSi}_2\text{O}_6]$, hedenbergite $[\text{CaFeSi}_2\text{O}_6]$ and jadeite $[\text{NaAlSi}_2\text{O}_6]$ are stable even at

Revision 2

309 very high pressures. Diopside retains its $C2/c$ symmetry to ~ 50 GPa at room
310 temperature and transforms to the β -CaMgSi₂O₆ phase at ~ 56 GPa (Chopelas and
311 Serghiou, 2002; Plonka et al., 2012). High pressure diffraction and Mössbauer studies
312 of hedenbergite also show that it is stable over 50 GPa until two discontinuities take
313 place at 53 and 68 GPa (Hu et al., 2015; Zhang et al., 1999). Jadeite is also stable at
314 high pressures to 30 GPa (Posner et al., 2014), and the jadeite-diopside solid solution
315 has no phase transition within pressure range of 0-47 GPa (Zhang et al., 2016).
316 Aegirine [NaFe³⁺Si₂O₆] also retains its symmetry to ~ 60 GPa, even though a
317 Na-coordination change induced isosymmetric phase transition takes place at ~ 24
318 GPa (Xu et al., 2016). Based on these studies one can expect that Ca and Na-rich
319 clinopyroxenes within the CaO-Na₂O-MgO-Fe^(2+/3+)O-Al₂O₃-SiO₂ system which are
320 important to the upper mantle and subduction zones, have large pressure ranges of
321 metastabilities (possibly 0-50 GPa at ambient temperature), however extensive studies
322 of the temperature effects are required (e.g., Nishihara et al., 2003; Zhao et al., 1998;
323 Zhao et al., 1997). Among the $C2/c$ clinopyroxenes augite is the most common and
324 occurs in various igneous rocks like basalt, gabbro and peridotite, and also in
325 metamorphic rocks like gneiss, schist and granulite (Banno, 1959; O'Har, 1961; Otten
326 and Buseck, 1987; Rooney et al., 2005; Schlinger and Veblen, 1989; Schorn and
327 Diener, 2016; Takeda et al., 1997; Tracy and Robinson, 1977). In this study the
328 diopside-rich augite was found to be metastable at simultaneously high pressure and
329 temperature to ~ 27 GPa and 700 K. Recently, the topic of metastable preservation of
330 pyroxenes to significant depths in cold slabs has attracted increasing attention, and is

Revision 2

331 treated as one of the explanations of the stagnations of some subducting slabs near the
332 base of the mantle transition zone (Agrusta et al., 2014; Bina, 2013; King et al., 2015;
333 Nishi et al., 2013; Van Mierlo et al., 2013). The main reason is that pyroxene is the
334 least dense mineral in the pyrolitic assemblage, and the density difference between the
335 slabs and surrounding mantle is a key factor that controls buoyancy, however, other
336 factors like viscosity also need to be considered (Agrusta et al., 2014; Nishi et al.,
337 2013). Pyroxenes can survive even at high temperatures, while in contrast, metastable
338 olivine can only persist under very cold conditions (Nishi et al., 2008; Nishi et al.,
339 2009). Even so, deciphering the effects of metastable pyroxenes on slab dynamics still
340 requires a lot of further measurements, including density and elasticity of relevant
341 minerals at simultaneous high-pressure and temperature conditions. However, such
342 work on pyroxenes is limited (e.g., Akashi et al., 2009; Nishihara et al., 2003; Zhao et
343 al., 1998; Zhao et al., 1997), and the pressure range is relatively low compared to
344 transition zone depth. In this study we conducted single-crystal X-ray diffraction
345 measurements on natural augite at simultaneously high-pressure and temperature to
346 ~27 GPa and 700 K, simulating conditions within the coldest part of a subducting slab.
347 The diffraction data reveal that augite is metastable within this range of P - T condition,
348 and the P - V - T data were used to calculate related thermoelastic parameters.

349 To date, numerous seismic studies on subducting slab morphology show that most
350 slabs are denser than the mantle before they sink into the transition zone depths,
351 where the densities of slabs and surrounding mantle become comparable (Figure 15).
352 However, depending on the slab geometry and thermal structure become different,

Revision 2

353 some subducted slabs sink into the lower mantle (e.g., Centre America), while others
354 stagnate (e.g., Tonga) (Fukao and Obayashi, 2013; Fukao et al., 2001; Grand, 2002;
355 Kawakatsu and Yoshioka, 2011; Li et al., 2008; Van der Hilst et al., 1997). Density is
356 the principle factor controlling buoyancy, and the metastable pyroxene is a candidate
357 contributor for slab stagnations (Agrusta et al., 2014; Bina, 2013; King et al., 2015;
358 Nishi et al., 2013; Van Mierlo et al., 2013). To better understand the effect of
359 metastable pyroxenes on the slab dynamics we calculated the density profiles of
360 augite and other common mantle pyroxene minerals along a geotherm that is typical
361 for cold subduction (Ganguly et al., 2009). The third order HTBM equation (formula
362 (1)-(4)) was used, and the minerals and related thermoelastic parameters are shown in
363 Table 7. The results comparing the PREM model (Dziewonski and Anderson, 1981)
364 and a Tonga-type slab (Ganguly et al., 2009) are presented in Figure 15. In this Figure
365 augite $[(Ca_{0.89}Na_{0.05}Mg_{0.06})(Mg_{0.74}Fe_{0.11}Al_{0.14}Ti_{0.01})(Si_{1.88}Al_{0.12})O_{6.00}]$ and aegirine
366 $[NaFe^{3+}Si_2O_6]$ are notably denser than other pyroxenes (jadeite $[NaAlSi_2O_6]$, diopside
367 $[CaMgSi_2O_6]$, omphacite $[Di_{63}Jd_{37}]$ and clinoenstatite $[Mg_2Si_2O_6]$) because of their
368 higher Fe contents. At depth above the transition zone these Fe-free pyroxenes have
369 densities closer to PREM pyrolite, while in the transition zone densities of augite and
370 aegirine are more comparable to the PREM. On the other hand, the Tonga-type slab is
371 significantly denser than all of these pyroxenes at depth below ~425 km. One could
372 conclude that the presence of the Fe-rich pyroxenes like augite and aegirine would
373 promote the sinking of slabs into the transition zone at the 410 km discontinuity. At
374 the 660 km boundary as the ringwoodite decomposes into much denser Mg-perovskite

Revision 2

375 and ferropericlasite (Green and Ringwood, 1967; Ito and Takahashi, 1989; Liu, 1976),
376 the slab and surrounding mantle densities become comparable, based on our
377 calculations all of these pyroxenes would contribute to the stagnation of the slab if
378 they are preserved in significant quantities.

379

380 **Acknowledgements**

381 This work was performed at GeoSoilEnviroCARS (Sector 13), Partnership for
382 Extreme Crystallography program (PX²), Advanced Photon Source (APS), and
383 Argonne National Laboratory. GeoSoilEnviroCARS is supported by the National
384 Science Foundation—Earth Sciences (EAR-1128799) and Department of
385 Energy—Geosciences (DE-FG02-94ER14466). PX² program is supported by
386 COMPRES under NSF Cooperative Agreement EAR 11-57758. Use of the
387 COMPRES-GSECARS gas loading system was supported by COMPRES under NSF
388 Cooperative Agreement EAR 11-57758 and by GSECARS. This project was
389 supported by the Strategic Priority Research Program (B) of the Chinese Academy of
390 Sciences (XDB 18010401), the National Natural Science Foundation of China (Grant
391 No. 41374107), the Joint Research Fund in Huge Scientific Equipment (U1632112)
392 under cooperative agreement between the National Natural Science Foundation of
393 China and Chinese Academy of Sciences and National Science Foundation under
394 grant EAR1344942. Development of the ATREX software used for data analysis is
395 supported by NSF grant EAR1440005. Use of the Advanced Photon Source was
396 supported by the US Department of Energy, Office of Science, Office of Basic

Revision 2

397 Energy Sciences, under Contract No.DE-AC02-06CH11357. J. Xu acknowledges
398 supports from Graduate Student Joint Training Program of the Institute of
399 Geochemistry, Chinese Academy of Sciences.

400

401 **References**

402 Agrusta, R., Hunen, J., and Goes, S. (2014) The effect of metastable pyroxene on the
403 slab dynamics. *Geophysical research letters*, 41(24), 8800-8808.

404 Akaogi, M., and Akimoto, S.-i. (1977) Pyroxene-garnet solid-solution equilibria in the
405 systems $Mg_4Si_4O_{12}$ - $Mg_3Al_2Si_3O_{12}$ and $Fe_4Si_4O_{12}$ - $Fe_3Al_2Si_3O_{12}$ at high
406 pressures and temperatures. *Physics of the Earth and Planetary Interiors*,
407 15(1), 90-106.

408 Akashi, A., Nishihara, Y., Takahashi, E., Nakajima, Y., Tange, Y., and Funakoshi,
409 K.i. (2009) Orthoenstatite/clinoenstatite phase transformation in $MgSiO_3$ at
410 high - pressure and high - temperature determined by in situ X - ray
411 diffraction: Implications for nature of the X discontinuity. *Journal of*
412 *Geophysical Research*, 114, B04206.

413 Aleksandrov, K., and Ryzhova, T. (1961) The elastic properties of rock forming
414 minerals, pyroxenes and amphiboles. *Izv. Acad. Sci. USSR, Geophys. Ser.* 9,
415 1339-1344.

416 Angel, R.J. (2000) Equations of state. *Reviews in mineralogy and geochemistry*,
417 41(1), 35-59.

418 Angel, R.J. (2015) Win_Strain Program for Strain Calculations

Revision 2

- 419 (<http://www.rossangel.net>).
- 420 Angel, R.J., Gonzalez-Platas, J., and Alvaro, M. (2014) EosFit7c and a Fortran
421 module (library) for equation of state calculations. *Zeitschrift Fur*
422 *Kristallographie*, 229(5), 405-419.
- 423 Banno, S. (1959) Aegirinaugites from crystalline schists in Sikoku. *Jour. Geol. Soc.*
424 *Japan*, 65(770).
- 425 Bina, C.R. (2013) Mineralogy: Garnet goes hungry. *Nature Geosci*, 6(5), 335-336.
- 426 Bindi, L., Safonov, O.G., Yapaskurt, V.O., Perchuk, L.L., and Menchetti, S. (2003)
427 Letter. Ultrapotassic clinopyroxene from the Kumdy-Kol microdiamond mine,
428 Kokchetav Complex, Kazakhstan: Occurrence, composition and
429 crystal-chemical characterization. *American Mineralogist*, 88(2-3), 464-468.
- 430 Chopelas, A., and Serghiou, G. (2002) Spectroscopic evidence for pressure-induced
431 phase transitions in diopside. *Physics and Chemistry of Minerals*, 29(6),
432 403-408.
- 433 Clark, J.R., Appleman, D.E., and Papike, J. (1969) Crystal-chemical characterization
434 of clinopyroxenes based on eight new structure refinements. *Mineralogical*
435 *Society of America Special Paper*, 2, 31-50.
- 436 Dera, P., Finkelstein, G.J., Duffy, T.S., Downs, R.T., Meng, Y., Prakapenka, V., and
437 Tkachev, S. (2013a) Metastable high-pressure transformations of
438 orthoferrosilite Fs 82. *Physics of the Earth and Planetary Interiors*, 221, 15-21.
- 439 Dera, P., Zhuravlev, K., Prakapenka, V., Rivers, M.L., Finkelstein, G.J.,
440 Grubor-Urosevic, O., Tschauer, O., Clark, S.M., and Downs, R.T. (2013b)

Revision 2

- 441 High pressure single-crystal micro X-ray diffraction analysis with
442 GSE_ADA/RSV software. High Pressure Research, 33(3), 466-484.
- 443 Dolomanov, O.V., Bourhis, L.J., Gildea, R.J., Howard, J.A., and Puschmann, H.
444 (2009) OLEX2: a complete structure solution, refinement and analysis
445 program. Journal of Applied Crystallography, 42(2), 339-341.
- 446 Downs, R.T. (2003) Topology of the pyroxenes as a function of temperature,
447 pressure, and composition as determined from the procrystal electron density.
448 American Mineralogist, 88(4), 556-566.
- 449 Downs, R.T., and Singh, A.K. (2006) Analysis of deviatoric stress from
450 nonhydrostatic pressure on a single crystal in a diamond anvil cell: The case of
451 monoclinic aegirine, NaFeSi₂O₆. Journal of Physics and Chemistry of Solids,
452 67(9-10), 1995-2000.
- 453 Dziewonski, A.M., and Anderson, D.L. (1981) Preliminary reference Earth model.
454 Physics of the earth and planetary interiors, 25(4), 297-356.
- 455 Fei, Y., Ricolleau, A., Frank, M., Mibe, K., Shen, G., and Prakapenka, V. (2007)
456 Toward an internally consistent pressure scale. Proceedings of the National
457 Academy of Sciences of the United States of America, 104(22), 9182-9186.
- 458 Finger, W., and Ohashi, N.Y. (1976) The thermal expansion of diopside to 800°C and
459 a refinement of the crystal structure at 700° c. American Mineralogist, 61,
460 303-310.
- 461 Finkelstein, G.J., Dera, P.K., Jahn, S., Oganov, A.R., Holl, C.M., Meng, Y., and
462 Duffy, T.S. (2014) Phase transitions and equation of state of forsterite to 90

Revision 2

- 463 GPa from single-crystal X-ray diffraction and molecular modeling. American
464 Mineralogist, 99(1), 35-43.
- 465 Frost, D.J. (2008) The Upper Mantle and Transition Zone. *Elements*, 4(3), 171-176.
- 466 Fukao, Y., and Obayashi, M. (2013) Subducted slabs stagnant above, penetrating
467 through, and trapped below the 660 km discontinuity. *Journal of Geophysical*
468 *Research: Solid Earth*, 118(11), 5920-5938.
- 469 Fukao, Y., Widiyantoro, S., and Obayashi, M. (2001) Stagnant slabs in the upper and
470 lower mantle transition region. *Reviews of Geophysics*, 39(3), 291-323.
- 471 Ganguly, J., Freed, A.M., and Saxena, S.K. (2009) Density profiles of oceanic slabs
472 and surrounding mantle: Integrated thermodynamic and thermal modeling, and
473 implications for the fate of slabs at the 660km discontinuity. *Physics of the*
474 *Earth and Planetary Interiors*, 172(3), 257-267.
- 475 Grand, S.P. (2002) Mantle shear-wave tomography and the fate of subducted slabs.
476 *Philosophical Transactions of the Royal Society of London A: Mathematical,*
477 *Physical and Engineering Sciences*, 360(1800), 2475-2491.
- 478 Green, D., and Ringwood, A. (1967) The stability fields of aluminous pyroxene
479 peridotite and garnet peridotite and their relevance in upper mantle structure.
480 *Earth and Planetary Science Letters*, 3, 151-160.
- 481 Hazen, R.M., and Finger, L.W. (1977) Compressibility and crystal structure of Angra
482 dos Reis fassaite to 52 kbar. *Carnegie Institution of Washington Year Book*,
483 76, 512-515.
- 484 Hu, Y., Dera, P., and Zhuravlev, K. (2015) Single-crystal diffraction and Raman

Revision 2

- 485 spectroscopy of hedenbergite up to 33 GPa. *Physics and Chemistry of*
486 *Minerals*, 42, 595-608.
- 487 Ito, E., and Takahashi, E. (1989) Postspinel transformations in the system Mg_2SiO_4
488 - Fe_2SiO_4 and some geophysical implications. *Journal of Geophysical*
489 *Research: Solid Earth*, 94(B8), 10637-10646.
- 490 Kantor, I., Prakapenka, V., Kantor, A., Dera, P., Kurnosov, A., Sinogeikin, S.,
491 Dubrovinskaia, N., and Dubrovinsky, L. (2012) BX90: A new diamond anvil
492 cell design for X-ray diffraction and optical measurements. *Review of*
493 *Scientific Instruments*, 83(12), 125102.
- 494 Kawakatsu, H., and Yoshioka, S. (2011) Metastable olivine wedge and deep dry cold
495 slab beneath southwest Japan. *Earth and Planetary Science Letters*, 303(1),
496 1-10.
- 497 King, S.D., Frost, D.J., and Rubie, D.C. (2015) Why cold slabs stagnate in the
498 transition zone. *Geology*, 43(3), 231-234.
- 499 Knight, K.S. (2010) Analytical expressions to determine the isothermal
500 compressibility tensor and the isobaric thermal expansion tensor for
501 monoclinic crystals: application to determine the direction of maximum
502 compressibility in jadeite. *Physics and Chemistry of Minerals*, 37(8), 529-533.
- 503 Levien, L., and Prewitt, C.T. (1981) High-pressure structural study of diopside.
504 *American Mineralogist*, 66(3-4), 315-323.
- 505 Li, C., van der Hilst, R.D., Engdahl, E.R., and Burdick, S. (2008) A new global model
506 for P wave speed variations in Earth's mantle. *Geochemistry, Geophysics,*

Revision 2

- 507 Geosystems, 9(5).
- 508 Liu, L.-G. (1976) The post-spinel phase of forsterite. *Nature* 262, 770 - 772.
- 509 McCarthy, A.C., Downs, R.T., and Thompson, R.M. (2008a) Compressibility trends
510 of the clinopyroxenes, and in-situ high-pressure single-crystal X-ray
511 diffraction study of jadeite. *American Mineralogist*, 93(1), 198-209.
- 512 McCarthy, A.C., Downs, R.T., Thompson, R.M., and Redhammer, G.J. (2008b) In
513 situ high-pressure single-crystal X-ray study of aegirine, $\text{NaFe}^{3+}\text{Si}_2\text{O}_6$, and the
514 role of M1 size in clinopyroxene compressibility. *American Mineralogist*,
515 93(11-12), 1829-1837.
- 516 Nestola, F., Ballaran, T.B., Liebske, C., Bruno, M., and Tribaudino, M. (2006)
517 High-pressure behaviour along the jadeite $\text{NaAlSi}_2\text{O}_6$ -aegirine $\text{NaFeSi}_2\text{O}_6$
518 solid solution up to 10 GPa. *Physics and Chemistry of Minerals*, 33(6),
519 417-425.
- 520 Nishi, M., Kato, T., Kubo, T., and Kikegawa, T. (2008) Survival of pyropic garnet in
521 subducting plates. *Physics of the Earth and Planetary Interiors*, 170(3),
522 274-280.
- 523 Nishi, M., Kubo, T., and Kato, T. (2009) Metastable transformations of eclogite to
524 garnetite in subducting oceanic crust. *Journal of mineralogical and*
525 *petrological sciences*, 104(3), 192-198.
- 526 Nishi, M., Kubo, T., Ohfuji, H., Kato, T., Nishihara, Y., and Irifune, T. (2013) Slow
527 Si–Al interdiffusion in garnet and stagnation of subducting slabs. *Earth and*
528 *Planetary Science Letters*, 361, 44-49.

Revision 2

- 529 Nishihara, Y., Takahashi, E., Matsukage, K., and Kikegawa, T. (2003) Thermal
530 equation of state of omphacite. *American Mineralogist*, 88(1), 80-86.
- 531 O'HAR, M. (1961) Petrology of the Scourie dyke, Sutherland. *Mineralogical*.
532 *Magazine*, 32, 848-865.
- 533 Ohashi Y. (1982) STRAIN, a program to calculate the strain tensor from two sets of
534 unit-cell parameters. In: Hazen R.M., Finger L.W, (eds.) *Comparative crystal*
535 *chemistry*, Wiley, New York, pp. 92- 102.
- 536 Otten, M.T., and Buseck, P.R. (1987) TEM study of the transformation of augite to
537 sodic pyroxene in eclogitized ferrogabbro. *Contributions to Mineralogy and*
538 *Petrology*, 96(4), 529-538.
- 539 Plonka, A.M., Dera, P., Irmen, P., Rivers, M.L., Ehm, L., and Parise, J.B. (2012) β -
540 diopside, a new ultrahigh - pressure polymorph of $\text{CaMgSi}_2\text{O}_6$ with six -
541 coordinated silicon. *Geophysical Research Letters*, 39(24).
- 542 Posner, E.S., Dera, P., Downs, R.T., Lazarz, J.D., and Irmen, P. (2014) High-pressure
543 single-crystal X-ray diffraction study of jadeite and kosmochlor. *Physics and*
544 *Chemistry of Minerals*, 41(9), 695-707.
- 545 Richet, P., Mysen, B.O., and Ingrin, J. (1998) High-temperature X-ray diffraction and
546 Raman spectroscopy of diopside and pseudowollastonite. *Physics and*
547 *Chemistry of Minerals*, 25(6), 401-414.
- 548 Ringwood, A.E. (1982) Phase transformations and differentiation in subducted
549 lithosphere: implications for mantle dynamics, basalt petrogenesis, and crustal
550 evolution. *The Journal of Geology*, 611-643.

Revision 2

- 551 Rivers, M., Prakapenka, V.B., Kubo, A., Pullins, C., Holl, C.M., and Jacobsen, S.D.
552 (2008) The COMPRES/GSECARS gas-loading system for diamond anvil
553 cells at the Advanced Photon Source. *High Pressure Research*, 28(3), 273-292.
- 554 Robinson, K., Gibbs, G., and Ribbe, P. (1971) Quadratic elongation: a quantitative
555 measure of distortion in coordination polyhedra. *Science*, 172(3983), 567-570.
- 556 Rooney, T.O., Furman, T., Yirgu, G., and Ayalew, D. (2005) Structure of the
557 Ethiopian lithosphere: Xenolith evidence in the Main Ethiopian Rift.
558 *Geochimica et Cosmochimica Acta*, 69(15), 3889-3910.
- 559 Schlinger, C.M., and Veblen, D.R. (1989) Magnetism and transmission electron
560 microscopy of Fe - Ti oxides and pyroxenes in a granulite from Lofoten,
561 Norway. *Journal of Geophysical Research: Solid Earth*, 94(B10),
562 14009-14026.
- 563 Schorn, S., and Diener, J.F. (2016) Details of the gabbro-to-eclogite transition
564 determined from microtextures and calculated chemical potential
565 relationships. *Journal of Metamorphic Geology*. doi: 10.1111/jmg.12220
- 566 Sheldrick, G.M. (2007) A short history of SHELX. *Acta Crystallographica Section A:*
567 *Foundations of Crystallography*, 64(1), 112-122.
- 568 Shinmei, T., Tomioka, N., Fujino, K., Kuroda, K., and Irifune, T. (1999) In situ X-ray
569 diffraction study of enstatite up to 12 GPa and 1473 K and equations of state.
570 *American Mineralogist*, 84, 1588-1594.
- 571 Takeda, H., Yugami, K., Bogard, D., and Miyamoto, M. (1997)
572 Plagioclase-augite-rich gabbro in the Caddo County IAB iron, and the missing

Revision 2

- 573 basalts associated with iron meteorites. Lunar and Planetary Science
574 Conference, 28, p. 409.
- 575 Thompson, R.M., and Downs, R.T. (2008) The crystal structure of diopside at
576 pressure to 10 GPa. American Mineralogist, 93(1), 177-186.
- 577 Tracy, R., and Robinson, P. (1977) Zoned titanian augite in alkali olivine basalt from
578 Tahiti and the nature of titanium substitutions in augite. American
579 Mineralogist, 62(7-8), 634-645.
- 580 Tribaudino, M., and Mantovani, L. (2014) Thermal expansion in C2/c pyroxenes: a
581 review and new high-temperature structural data for a pyroxene of
582 composition $(\text{Na}_{0.53}\text{Ca}_{0.47})(\text{Al}_{0.53}\text{Fe}_{0.47})\text{Si}_2\text{O}_6$ (Jd(53)Hd(47)). Mineralogical
583 Magazine, 78(2), 311-324.
- 584 Tribaudino, M., Nestola, F., Bruno, M., Ballaran, T.B., and Liebske, C. (2008)
585 Thermal expansion along the $\text{NaAlSi}_2\text{O}_6$ - $\text{NaFe}^{(3+)}\text{Si}_2\text{O}_6$ and
586 $\text{NaAlSi}_2\text{O}_6$ - $\text{CaFe}^{(2+)}\text{Si}_2\text{O}_6$ solid solutions. Physics and Chemistry of
587 Minerals, 35(5), 241-248.
- 588 Ullrich, A., Miletich, R., Balic-Zunic, T., Olsen, L., Nestola, F., Wildner, M., and
589 Ohashi, H. (2010) $(\text{Na}, \text{Ca})(\text{Ti}^{3+}, \text{Mg})\text{Si}_2\text{O}_6$ -clinopyroxenes at high pressure:
590 influence of cation substitution on elastic behavior and phase transition.
591 Physics and Chemistry of Minerals, 37(1), 25-43.
- 592 Van der Hilst, R., Widiyantoro, S., and Engdahl, E. (1997) Evidence for deep mantle
593 circulation from global tomography. Nature, 386, 578-584.
- 594 Van Mierlo, W., Langenhorst, F., Frost, D., and Rubie, D. (2013) Stagnation of

Revision 2

- 595 subducting slabs in the transition zone due to slow diffusion in majoritic
596 garnet. *Nature Geoscience*, 6(5), 400-403.
- 597 Xu, J., Kuang, Y., Zhang, B., Liu, Y., Fan, D., Li, X., and Xie, H. (2016) Thermal
598 equation of state of natural tourmaline at high pressure and temperature.
599 *Physics and Chemistry of Minerals*, 43(5), 315-326.
- 600 Xu, J., Zhang, D., Fan, D., Downs, R.T., Hu, Y., Dera, P. (2016) Isosymmetric
601 pressure-induced bonding increase changes compression behavior of
602 clinopyroxenes across jadeite-aegirine solid solution in subduction zones.
603 *Journal of Geophysical Research: Solid Earth* (Under review)
- 604 Yang, H., and Prewitt, C.T. (2000) Chain and layer silicates at high temperatures and
605 pressures. *Reviews in Mineralogy and Geochemistry*, 41(1), 211-255.
- 606 Zhang, D., Hu, Y., and Dera, P.K. (2016) Compressional behavior of omphacite to
607 47 GPa. *Physics and Chemistry of Minerals*, 1-9.
- 608 Zhang, J.S., Dera, P., and Bass, J.D. (2012) A new high-pressure phase transition in
609 natural Fe-bearing orthoenstatite. *American Mineralogist*, 97(7), 1070-1074.
- 610 Zhang, L., Ahsbahs, H., Hafner, S.S., and Kutoglu, A. (1997) Single-crystal
611 compression and crystal structure of clinopyroxene up to 10 GPa. *American*
612 *Mineralogist*, 82(3), 245-258.
- 613 Zhang, L., Stanek, J., Hafner, S., Ahsbahs, H., Grünsteudel, H., and Metge, J. (1999)
614 ⁵⁷Fe nuclear forward scattering of synchrotron radiation in hedenbergite
615 CaFeSi₂O₆ at hydrostatic pressures up to 68 GPa. *American Mineralogist*,
616 84(3), 447-453.

Revision 2

617 Zhao, Y., Dreele, R.V., Zhang, J., and Weidner, D. (1998) Thermoelastic Equation of
618 State of Monoclinic Pyroxene: CaMgSi₂O₆ Diopside. The Review of High
619 Pressure Science and Technology, 7, 25-27.

620 Zhao, Y., Von Dreele, R.B., Shankland, T.J., Weidner, D.J., Zhang, J., Wang, Y., and
621 Gasparik, T. (1997) Thermoelastic equation of state of jadeite NaAlSi₂O₆: An
622 energy - dispersive Reitveld Refinement Study of low symmetry and multiple
623 phases diffraction. Geophysical Research Letters, 24(1), 5-8.

624

625

626 **Figure 1** Normalized unit cell volume and lattice parameters (*a*, *b* and *c*) of augite as
627 a function of pressure at room temperature. The error bars of the data points are
628 smaller than the symbols.

629 **Figure 2** Pressure dependence of β angle at ambient temperature. The error bars of
630 the data points are smaller than the symbols.

631 **Figure 3** Eulerian strain-normalized pressure (F_E-f_E) plot of unit cell volume.

632 **Figure 4** The orientation of the representation quadric for the isothermal
633 compressibility tensor of augite at 26.65 GPa, viewd down *b*.

634 **Figure 5** Pressure dependences of *M1O*₆, *M2O*₈ and *TO*₄ polyhedral volumes. The
635 error bars of the data points are smaller than the symbols.

636 **Figure 6** Pressure dependences of the polyhedral and unit-cell volumes. The error
637 bars of the data points are smaller than the symbols.

638 **Figure 7** Pressure dependences of distortion indices of different polyhedral.

Revision 2

- 639 **Figure 8** Pressure dependences of the $M2$ -O bond lengths in $M2O_8$ polyhedron.
- 640 **Figure 9** Pressure dependences of the $M1$ -O bond lengths in $M1O_6$ polyhedron
- 641 **Figure 10** An illustration of the O3-O3-O3 angle.
- 642 **Figure 11** Tetrahedral chains kinking as described by O3-O3-O3 angle as a function
- 643 of pressure.
- 644 **Figure 12** The unit-cell volume as a function of pressure and temperature.
- 645 **Figure 13** Polyhedral volumes as a function of pressure in jadeite (Posner et al., 2014),
- 646 aegirine (McCarthy et al., 2008b), hedenbergite (Zhang et al., 1997), diopside
- 647 (Thompson and Downs, 2008) and augite (This study). (a), (b) and (c) are
- 648 $M2$ -polyhedron, $M1$ -octahedron and T -tetrahedron, respectively.
- 649 **Figure 14** Pressure dependences of the T -O bond lengths in TO_4 polyhedron.
- 650 **Figure 15** Calculated density profiles of augite as well as other common
- 651 clinopyroxenes to ~800 km, and the PREM (Dziewonski and Anderson, 1981) model
- 652 and the density profile of a Tonga-type slab (Ganguly et al., 2009) are also showed.
- 653 (*Color online*).

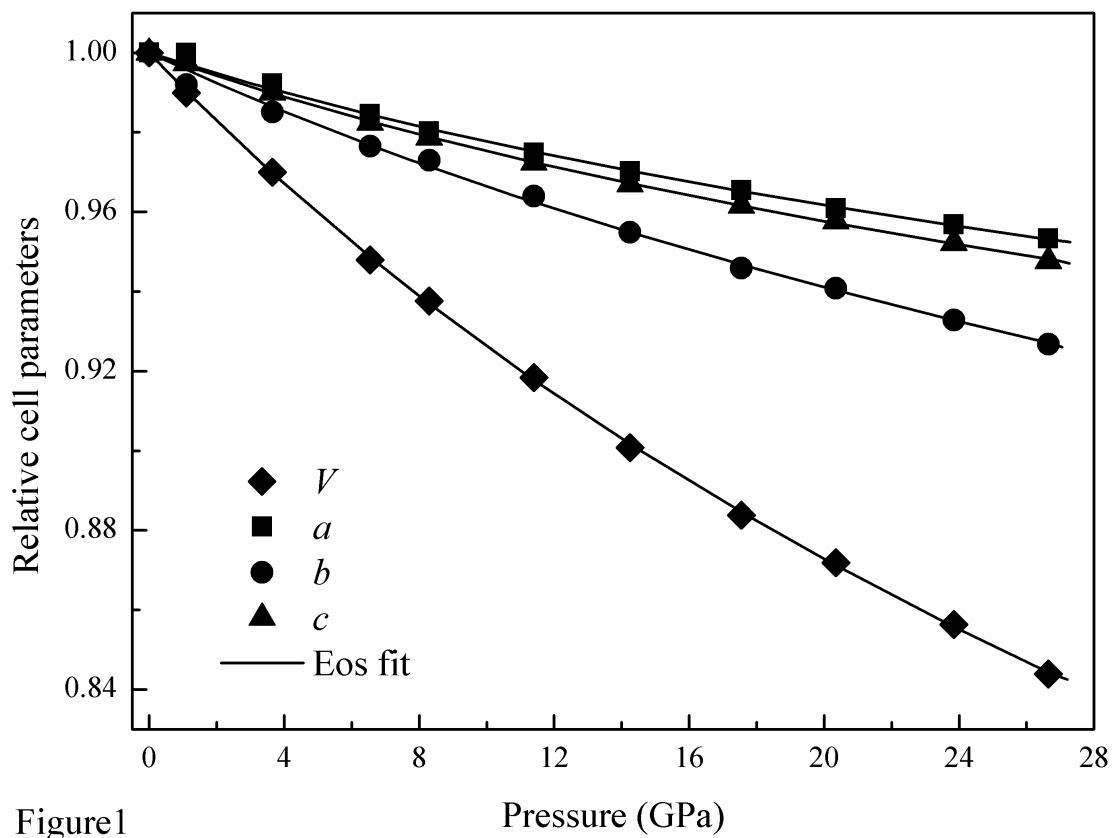


Figure 1

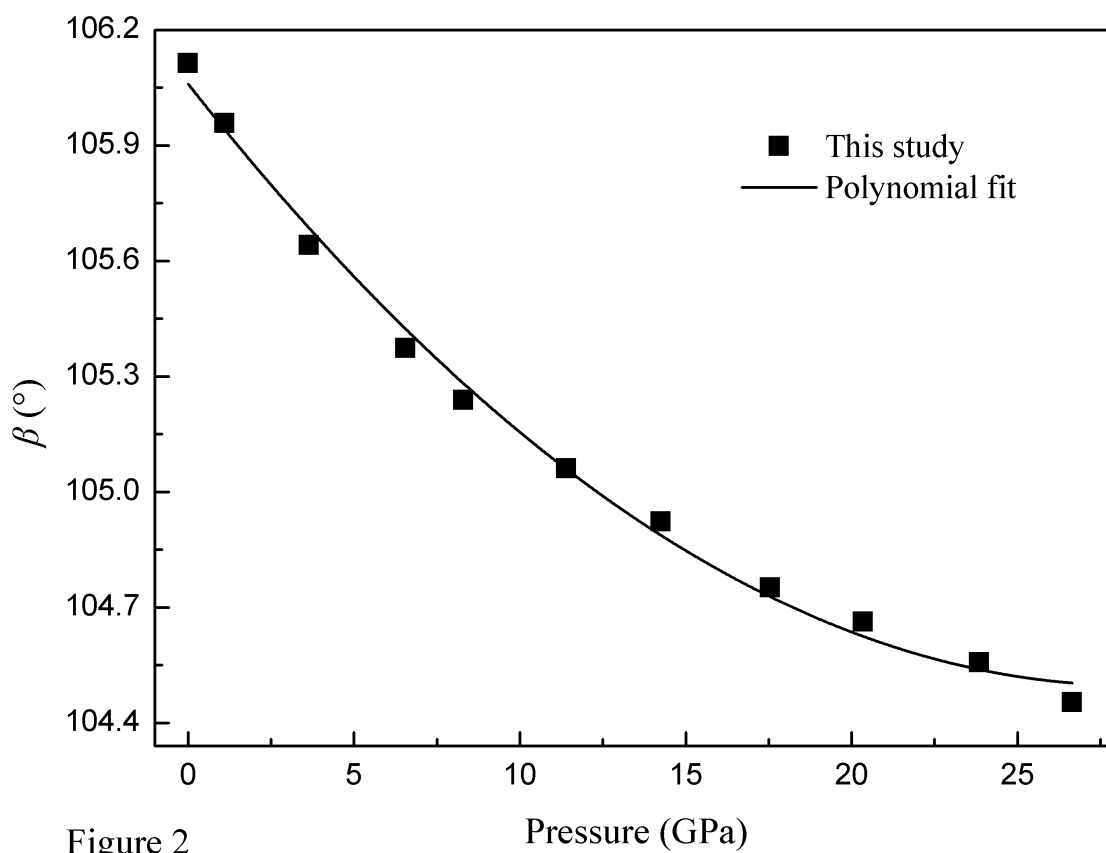


Figure 2

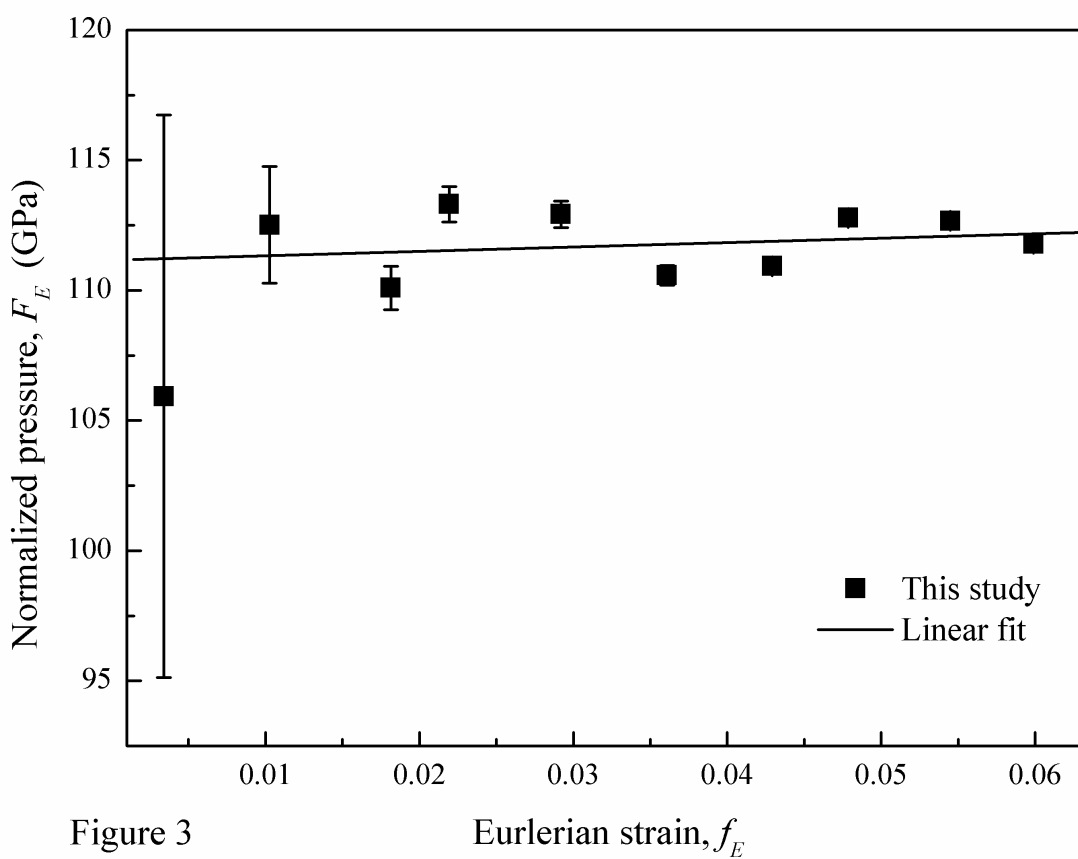


Figure 3

Eulerian strain, f_E

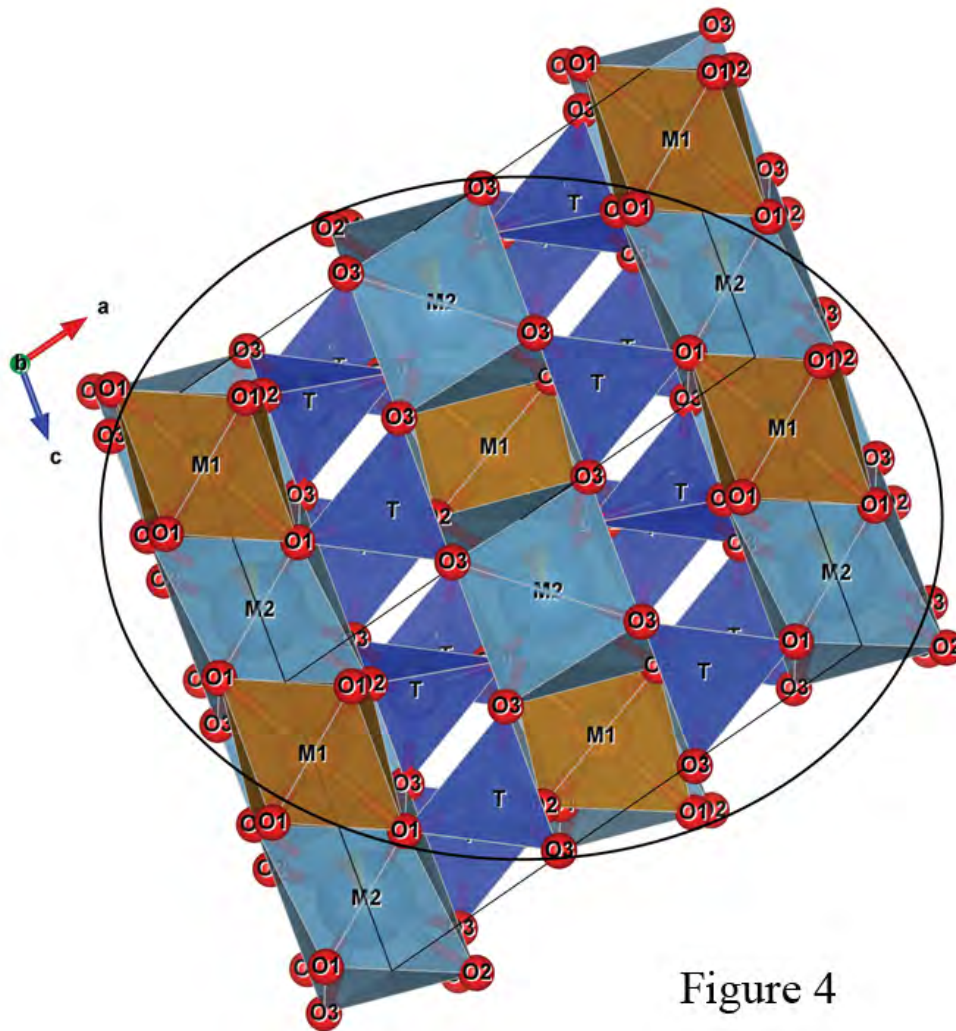


Figure 4

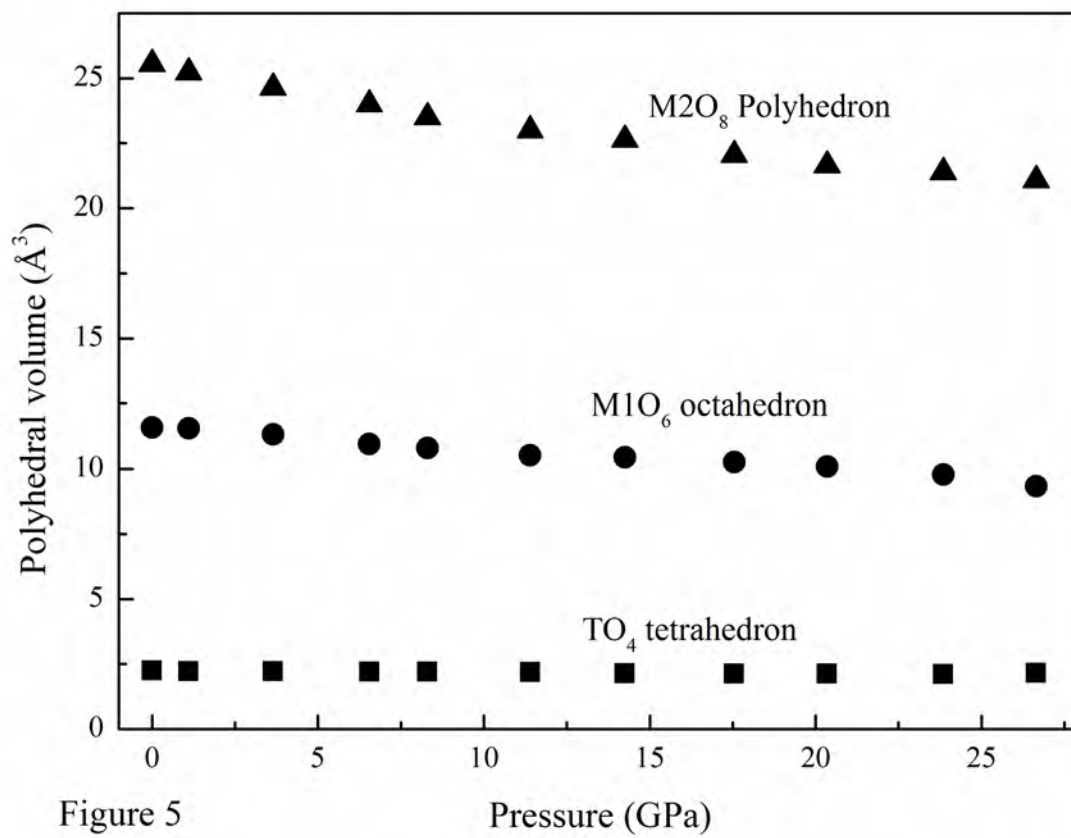


Figure 5

Pressure (GPa)

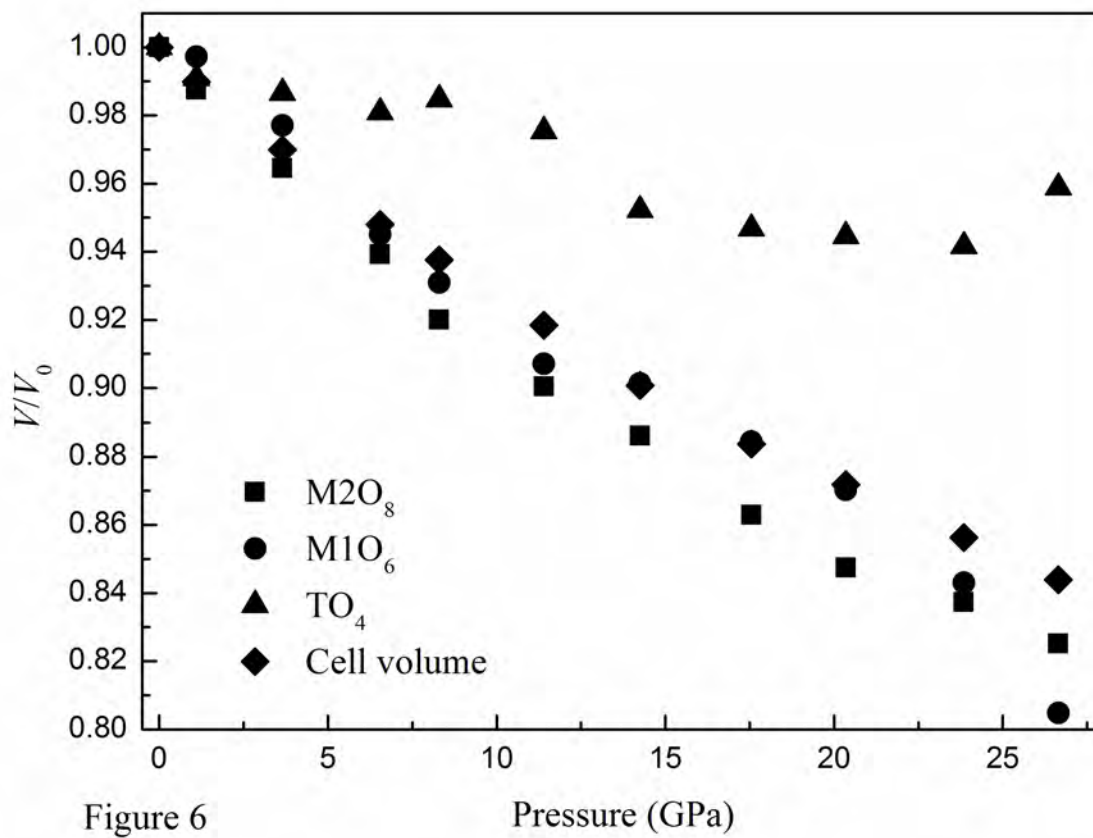
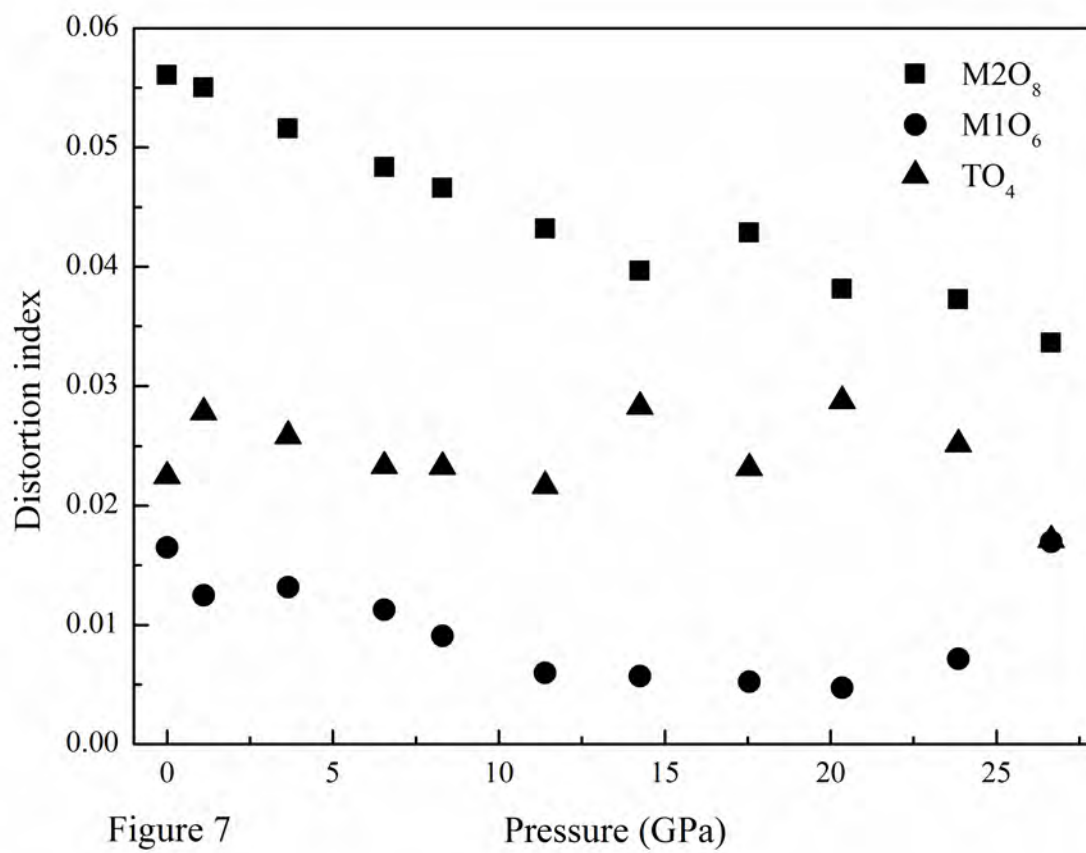


Figure 6

Pressure (GPa)



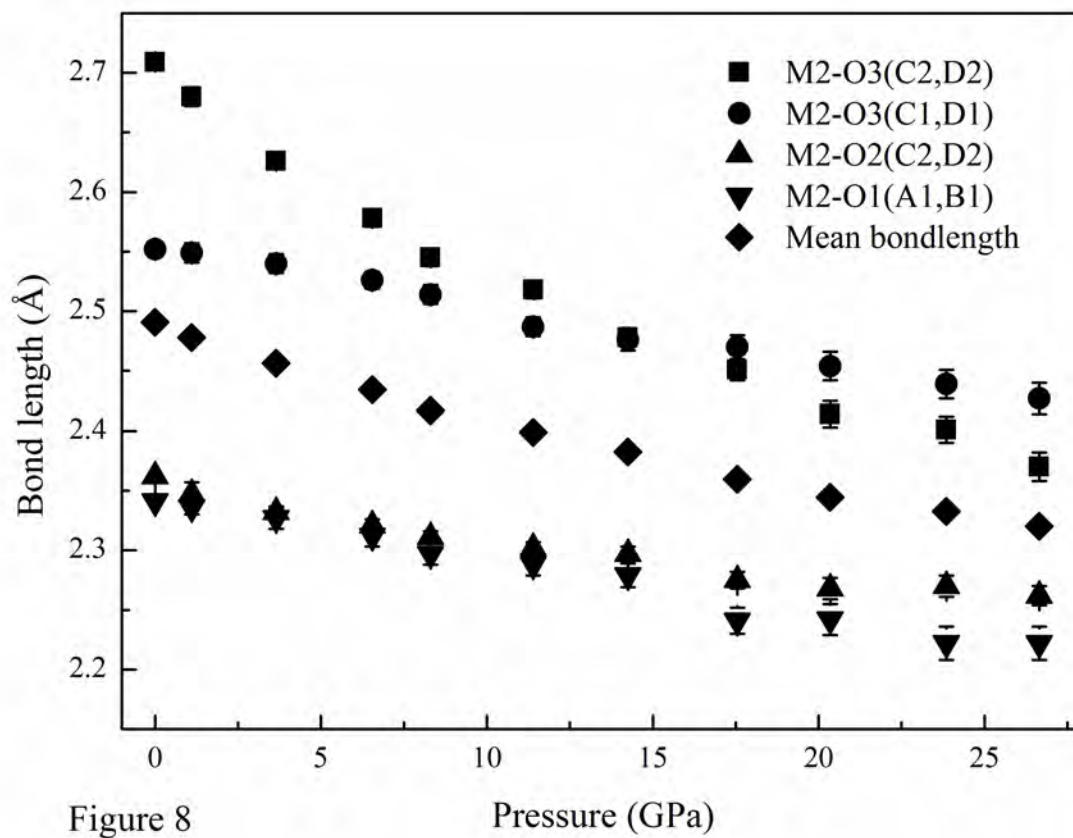


Figure 8

Pressure (GPa)

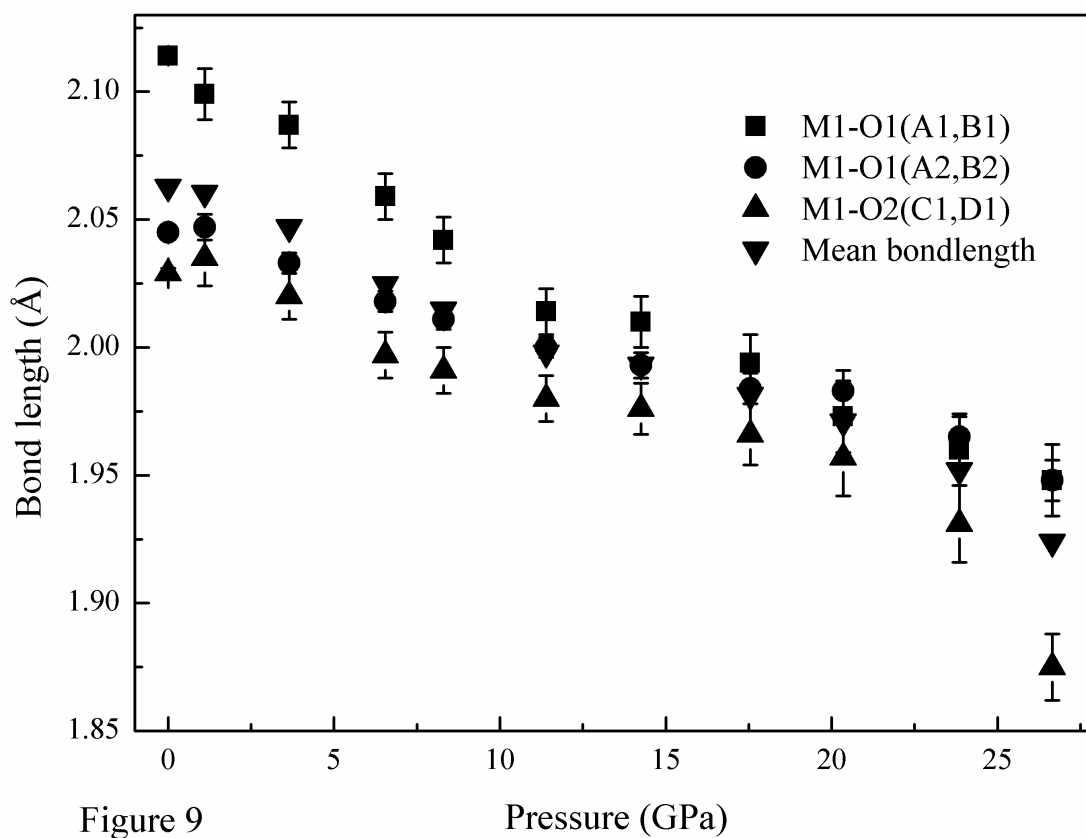


Figure 9

Pressure (GPa)

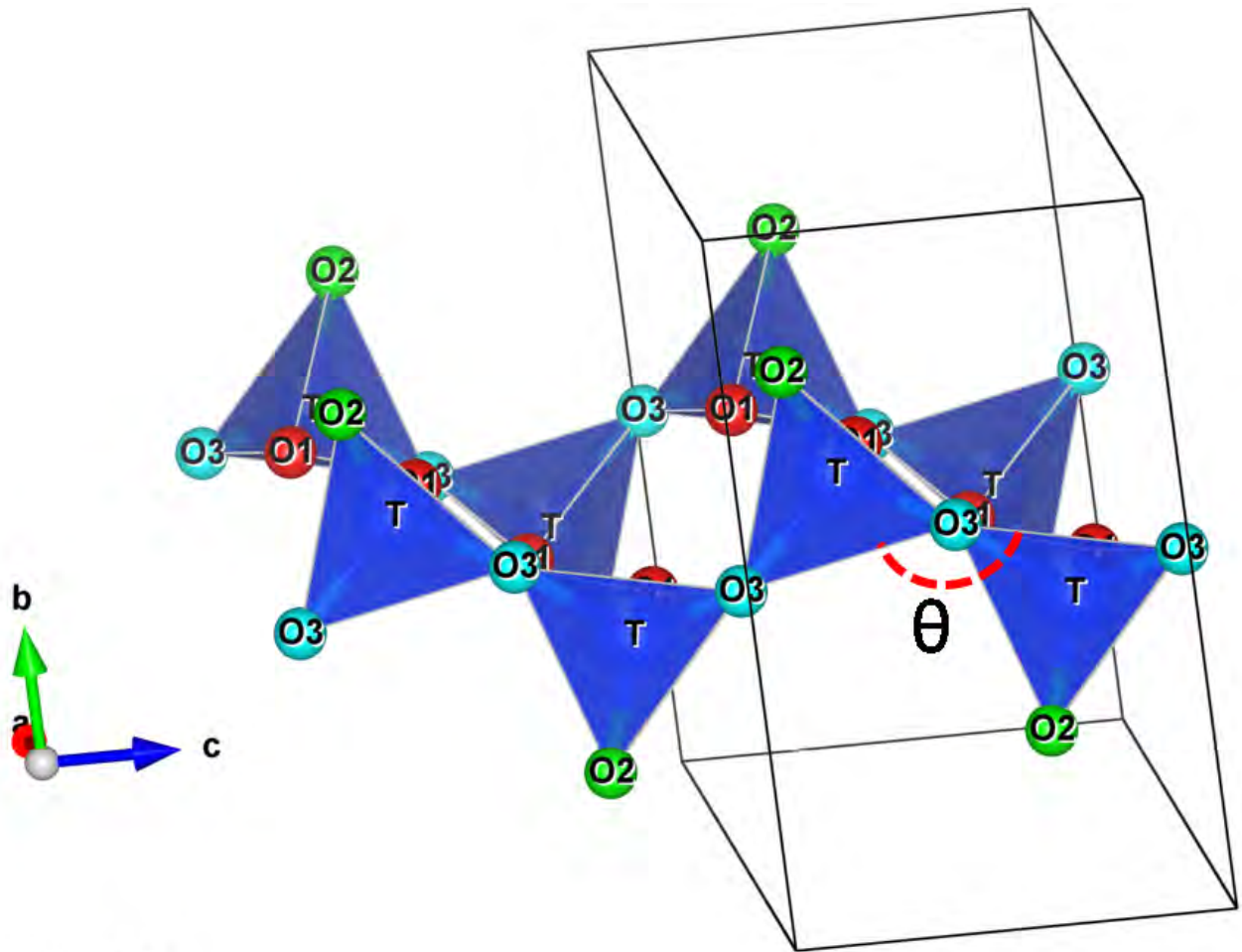


Figure 10

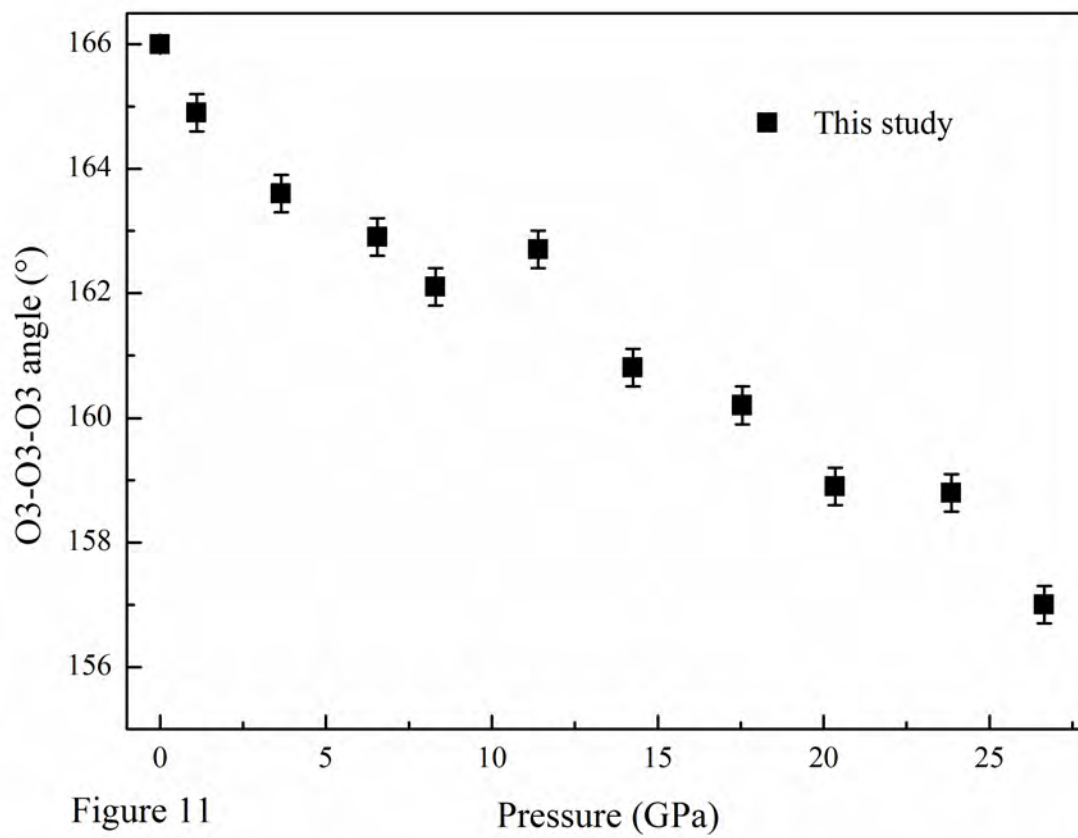
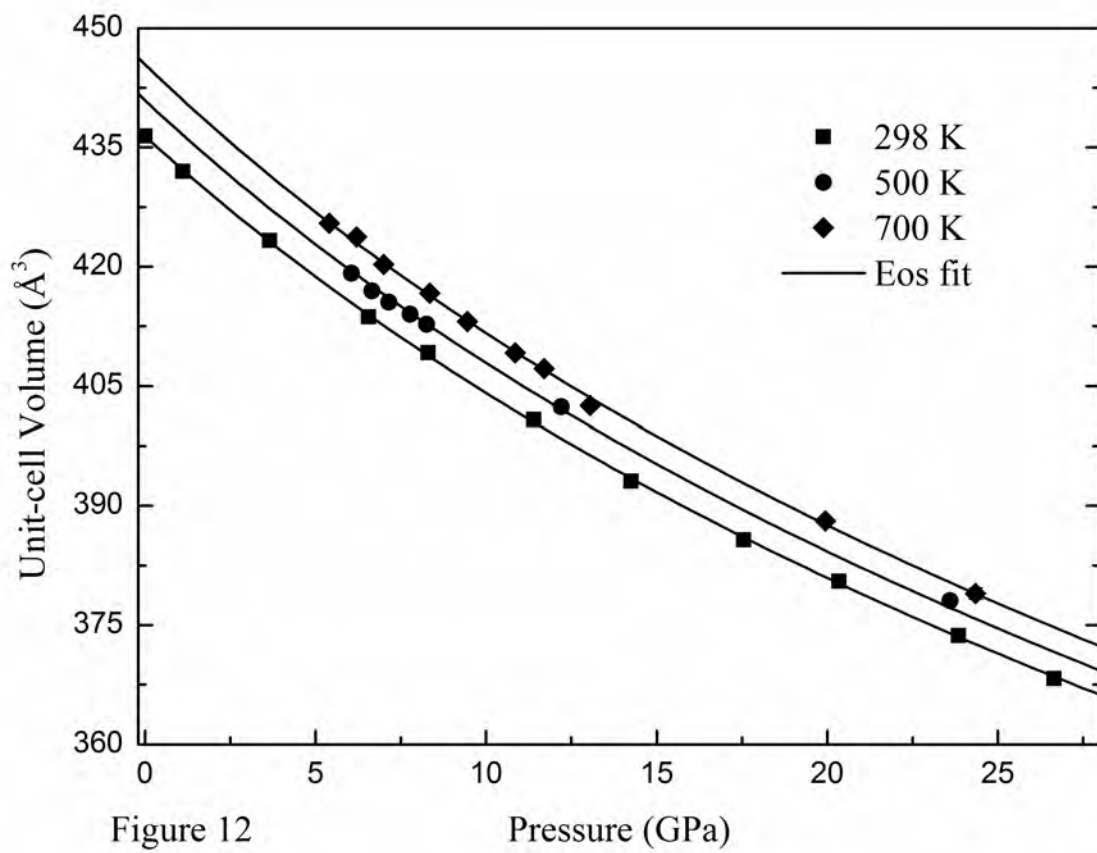


Figure 11

Pressure (GPa)



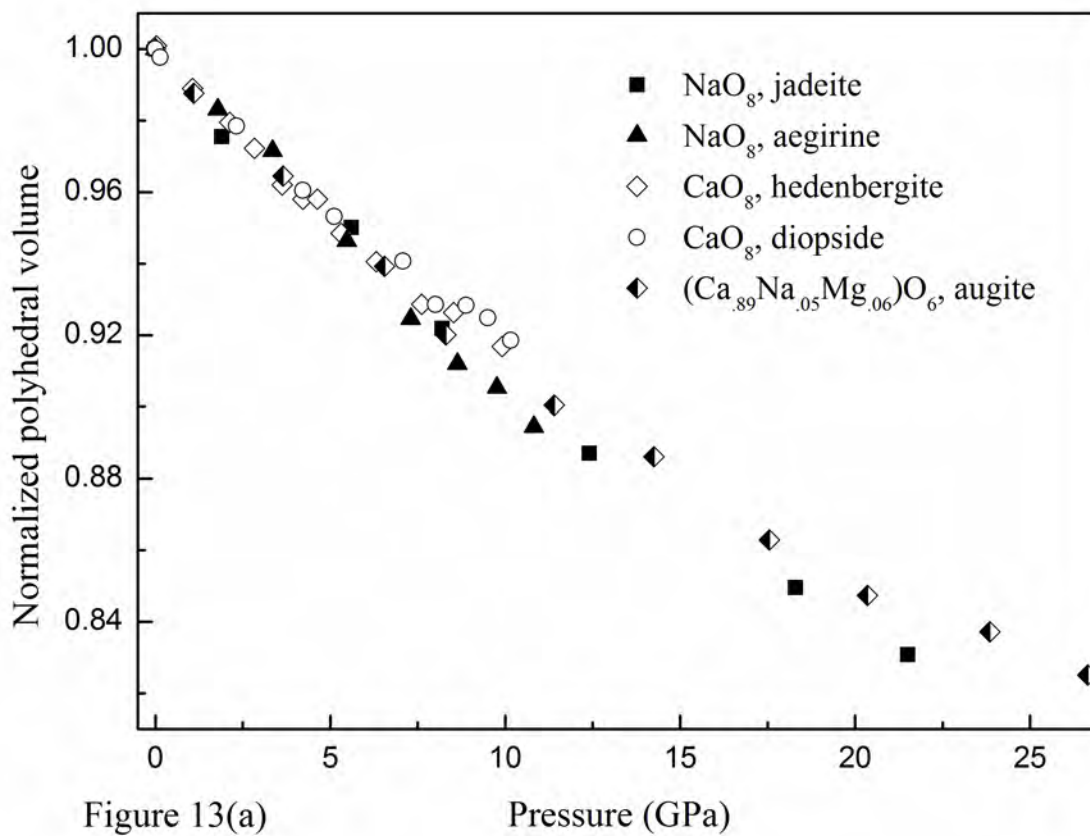
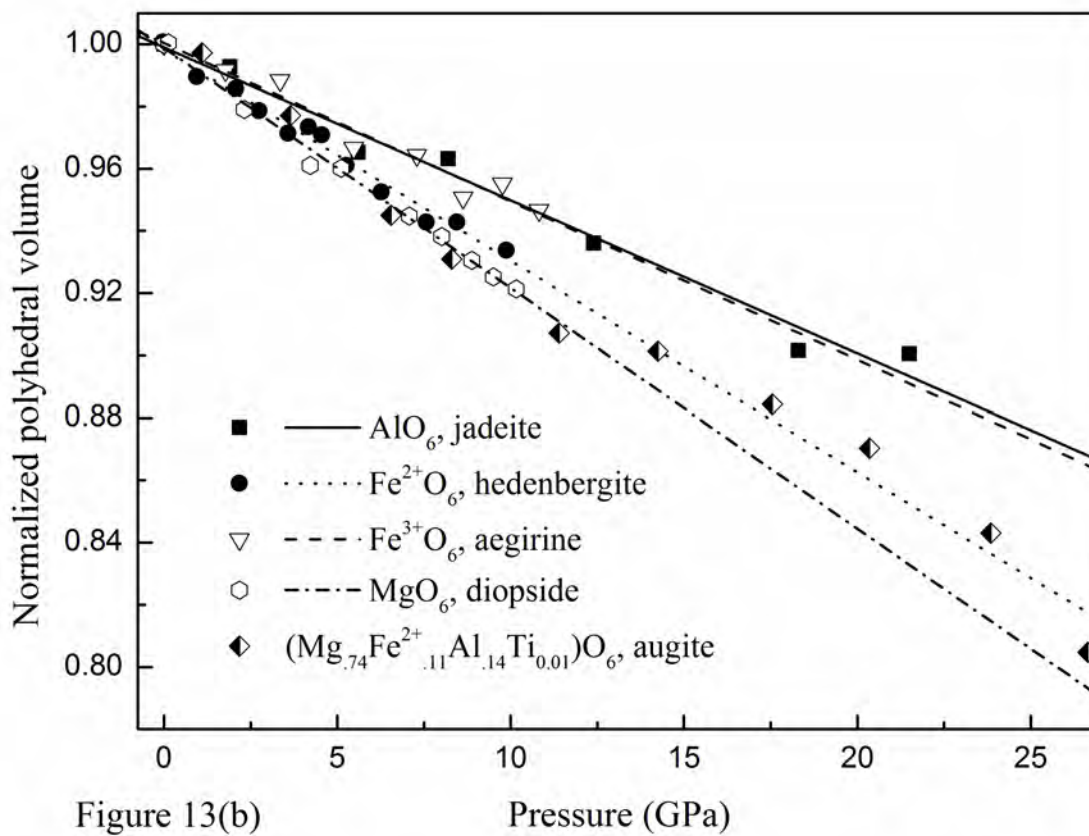
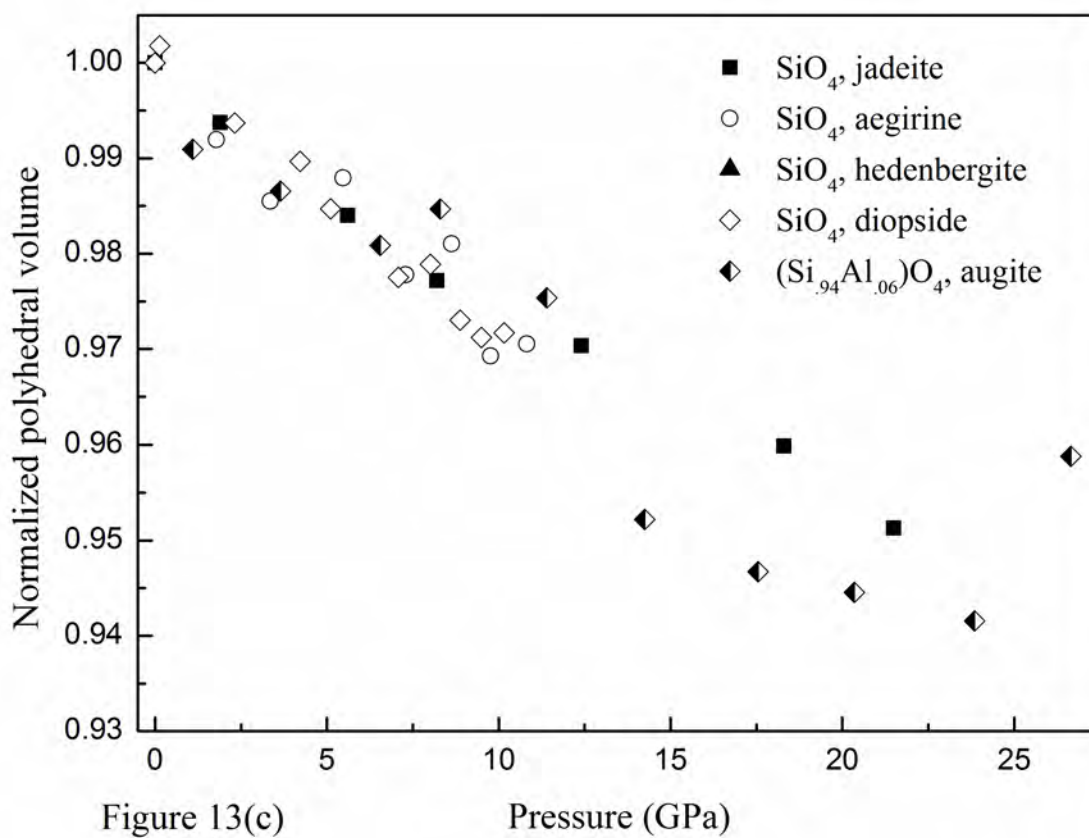


Figure 13(a)

Pressure (GPa)





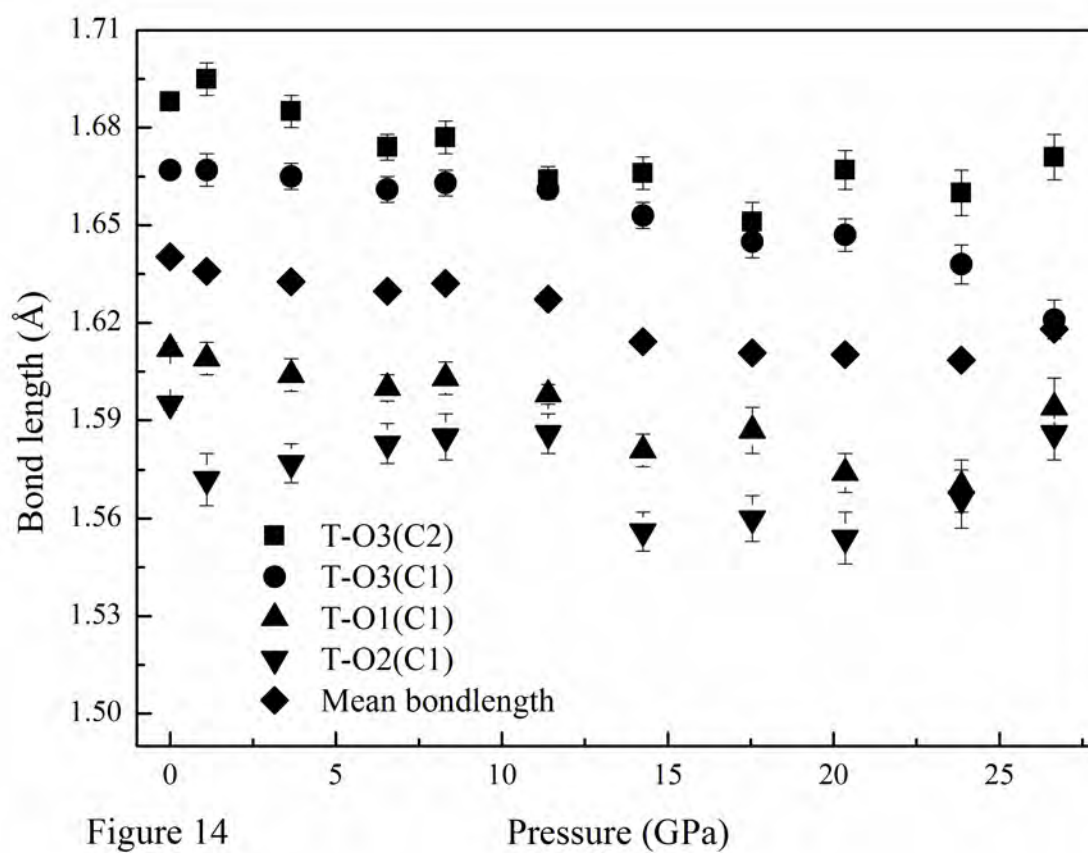


Figure 14

Pressure (GPa)

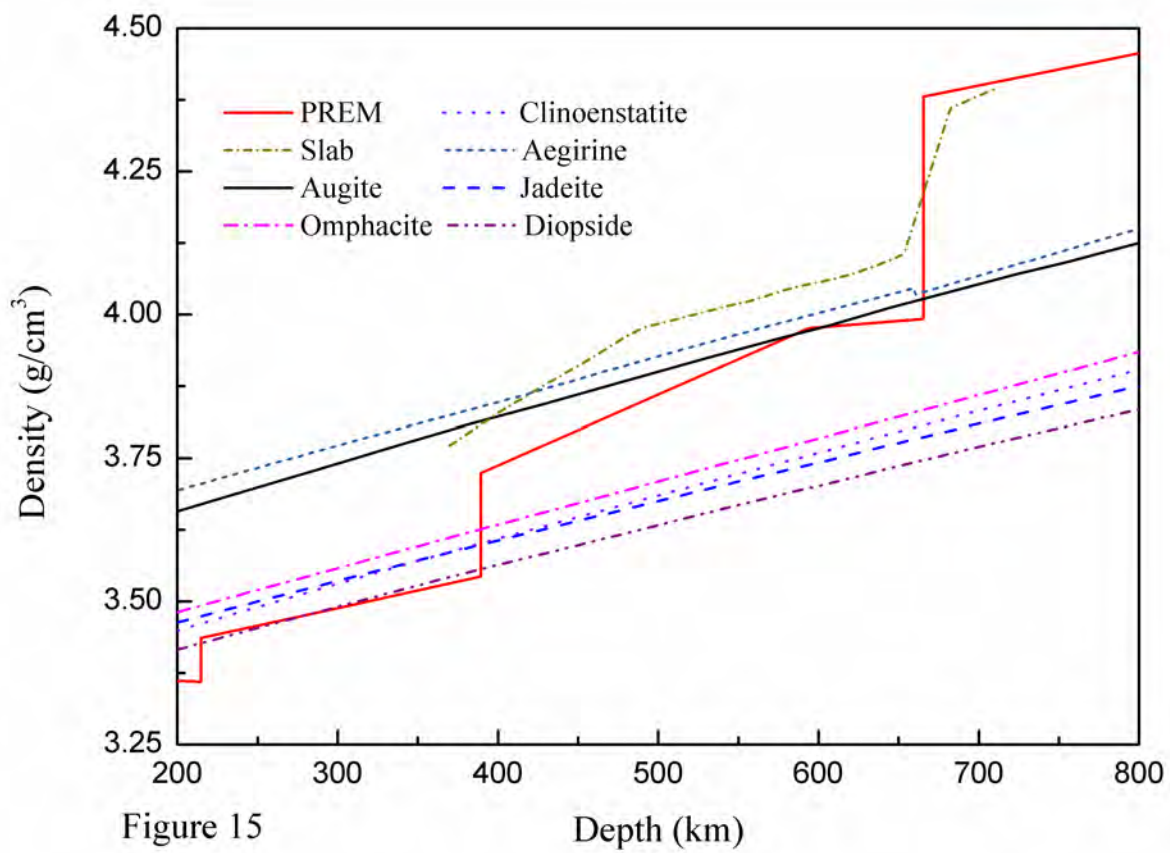


Figure 15

Depth (km)

Table 1 Unit cell parameters and densities of augite at various temperatures and pressures

<i>T</i> (K)	<i>P</i> (GPa)	<i>a</i> (Å)	<i>b</i> (Å)	<i>c</i> (Å)	β (°)	<i>V</i> (Å ³)	ρ (g/cm ³)
298	0.0001	9.719(1)	8.880(1)	5.2636(4)	106.11(1)	436.4(1)	3.327
298	1.05(5)	9.718(3)	8.808(4)	5.2497(7)	105.96(1)	432.0(3)	3.361
298	3.65(7)	9.644(3)	8.747(4)	5.2108(7)	105.64(1)	423.3(2)	3.430
298	6.55(4)	9.569(3)	8.671(4)	5.1712(7)	105.37(1)	413.7(2)	3.510
298	8.30(4)	9.527(3)	8.640(4)	5.1516(7)	105.24(1)	409.2(2)	3.549
298	11.40(3)	9.474(3)	8.560(4)	5.1184(7)	105.06(1)	400.8(2)	3.623
298	14.25(2)	9.429(3)	8.479(4)	5.0894(7)	104.92(1)	393.1(2)	3.694
298	17.55(1)	9.383(3)	8.399(4)	5.0615(7)	104.75(1)	385.7(2)	3.765
298	20.35(2)	9.339(3)	8.354(4)	5.0409(7)	104.66(1)	380.5(2)	3.816
298	23.85(1)	9.300(3)	8.283(4)	5.0120(7)	104.56(1)	373.7(2)	3.886
298	26.65(2)	9.265(3)	8.229(4)	4.9882(7)	104.45(1)	368.3(2)	3.943
500	6.05(2)	9.613(4)	8.740(8)	5.1876(23)	105.88(5)	419.2(5)	3.464
500	6.65(2)	9.600(4)	8.720(7)	5.1809(21)	105.96(5)	417.0(4)	3.482
500	7.15(1)	9.596(4)	8.710(4)	5.1725(19)	106.01(4)	415.5(4)	3.495
500	7.78(2)	9.550(4)	8.697(6)	5.1679(15)	105.30(3)	414.0(4)	3.508
500	8.25(1)	9.577(4)	8.688(9)	5.1612(20)	106.04(5)	412.7(5)	3.519
500	12.20(2)	9.460(3)	8.638(13)	5.1204(13)	105.22(2)	402.4(6)	3.609
500	23.60(1)	9.326(5)	8.453(23)	5.0101(18)	106.82(3)	378.1(4)	3.841
700	5.40(1)	9.615(3)	8.816(6)	5.2162(7)	105.79(1)	425.5(3)	3.413
700	6.20(3)	9.578(3)	8.825(6)	5.2064(8)	105.67(1)	423.7(3)	3.427
700	7.00(3)	9.592(3)	8.770(6)	5.1947(6)	105.90(1)	420.3(3)	3.455
700	8.35(4)	9.568(3)	8.749(6)	5.1782(6)	106.00(1)	416.7(3)	3.485
700	9.45(5)	9.520(4)	8.710(6)	5.1664(7)	105.33(1)	413.1(3)	3.515

700	10.85(3)	9.495(3)	8.675(4)	5.1484(6)	105.24(1)	409.2(2)	3.549
700	11.70(3)	9.525(4)	8.659(5)	5.1407(7)	106.17(1)	407.2(3)	3.566
700	13.05(1)	9.471(4)	8.594(7)	5.121(16)	105.03(3)	402.5(4)	3.608
700	19.95(2)	9.432(3)	8.485(10)	5.0558(14)	106.42(2)	388.1(5)	3.742
700	24.35(1)	9.302(4)	8.386(16)	5.0217(18)	104.67(3)	379.0(7)	3.831

Table 2 Structural refinement details of augite at different pressures to 26.65 GPa

Pressure (GPa)	0.0001	1.05(5)	3.65(7)	6.55(4)	8.30(4)	11.40(3)
R_{int} (%)	5.19	7.21	6.24	5.57	5.75	5.56
R_1 (all reflections, %)	3.69	3.77	3.82	3.40	2.93	2.61
R_1 ($F_o > 4\text{sig}(F_o)$, %)	3.69	3.77	3.82	3.40	2.93	2.61
wR_2 (all reflections, %)	9.35	10.31	9.45	8.92	7.52	6.69
Goodness of fit	1.052	1.073	0.996	1.061	1.067	1.047
No. of total reflections	3196	564	625	592	556	537
No. of reflections ($F_o > 4\text{sig}(F_o)$)	749	181	197	182	154	145
No. of fitting parameters	32	32	32	32	32	32
Pressure (GPa)	14.25(2)	17.55(1)	20.35(2)	23.85(1)	26.65(2)	
R_{int} (%)	5.50	6.31	5.85	5.34	7.20	
R_1 (all reflections, %)	3.46	4.26	3.23	4.02	4.23	
R_1 ($F_o > 4\text{sig}(F_o)$, %)	3.46	4.22	3.23	4.02	4.23	
wR_2 (all reflections, %)	8.22	9.98	7.61	9.96	10.51	
Goodness of fit	1.091	1.062	1.077	1.032	1.030	
No. of total reflections	534	509	487	501	488	
No. of reflections ($F_o > 4\text{sig}(F_o)$)	142	128	113	117	105	
No. of fitting parameters	32	32	32	32	32	

Table 3 Fractional coordinates and displacement parameters of atoms in augite at different pressures

Pressure (GPa)	0.0001	1.05(5)	3.65(7)	6.55(4)	8.30(4)	11.40(3)	14.25(2)	17.55(1)	20.35(2)	23.85(1)	26.65(2)
M2											
x	0	0	0	0	0	0	0	0	0	0	0
y	0.30145(8)	0.3018(3)	0.3028(3)	0.3038(3)	0.3049(3)	0.3056(2)	0.3070(3)	0.3076(4)	0.3085(3)	0.3093(4)	0.3105(4)
z	0.2500	0.2500	0.2500	0.2500	0.2500	0.2500	0.2500	0.2500	0.2500	0.2500	0.2500
Uiso	0.0102(2)	0.0134(8)	0.0129(7)	0.0123(6)	0.0123(8)	0.0132(8)	0.0085(7)	0.0093(9)	0.0090(7)	0.0118(8)	0.0110(11)
M1											
x	0	0	0	0	0	0	0	0	0	0	0
y	0.9074(1)	0.9079(5)	0.9083(4)	0.9091(4)	0.9105(4)	0.9111(3)	0.9109(4)	0.9117(6)	0.9121(5)	0.9117(5)	0.9107(7)
z	0.2500	0.2500	0.2500	0.2500	0.2500	0.2500	0.2500	0.2500	0.2500	0.2500	0.2500
Uiso	0.0090(2)	0.0143(11)	0.0134(9)	0.0127(9)	0.0154(11)	0.0163(10)	0.0104(8)	0.0119(10)	0.0112(10)	0.0108(10)	0.0129(13)
T											
x	0.28717(7)	0.2867(2)	0.2869(2)	0.2869(2)	0.2868(2)	0.2867(1)	0.2865(2)	0.2866(3)	0.2860(2)	0.2848(3)	0.2863(3)
y	0.09319(6)	0.0944(3)	0.0944(2)	0.0947(2)	0.0953(3)	0.0958(2)	0.0965(3)	0.0966(3)	0.0975(3)	0.0980(3)	0.0989(4)
z	0.2290(1)	0.2281(2)	0.2278(2)	0.2270(2)	0.2273(2)	0.2273(2)	0.2277(2)	0.2287(3)	0.2285(3)	0.2287(3)	0.2303(4)
Uiso	0.0066(1)	0.0097(7)	0.0102(6)	0.0103(7)	0.0121(8)	0.0095(7)	0.0081(6)	0.0093(8)	0.0097(7)	0.0096(10)	0.0100(10)
O1											
x	0.1147(2)	0.1146(5)	0.1143(5)	0.1135(4)	0.1125(5)	0.1122(3)	0.1132(5)	0.1118(7)	0.1120(5)	0.1106(7)	0.1098(8)
y	0.0865(2)	0.0868(8)	0.0880(7)	0.0878(6)	0.0889(8)	0.0879(6)	0.0887(6)	0.0909(7)	0.0898(6)	0.0904(8)	0.0895(9)
z	0.1397(3)	0.1405(7)	0.1398(5)	0.1393(6)	0.1394(5)	0.1393(4)	0.1391(7)	0.1396(9)	0.1408(7)	0.1396(8)	0.1379(10)
Uiso	0.0095(3)	0.0094(9)	0.0093(7)	0.0100(7)	0.0095(7)	0.0091(6)	0.0084(8)	0.0093(11)	0.0108(11)	0.0115(14)	0.0082(16)
O2											
x	0.3619(2)	0.3610(7)	0.3592(5)	0.3591(5)	0.3592(6)	0.3577(4)	0.3568(5)	0.3567(7)	0.3564(6)	0.3554(6)	0.3577(7)
y	0.2517(2)	0.2512(8)	0.2539(7)	0.2563(6)	0.2576(8)	0.2602(7)	0.2591(6)	0.2609(7)	0.2618(7)	0.2654(9)	0.2710(11)
z	0.3192(4)	0.3203(8)	0.3216(6)	0.3230(6)	0.3249(6)	0.3273(4)	0.3269(6)	0.3314(8)	0.3324(7)	0.3327(8)	0.3346(10)
Uiso	0.0113(3)	0.0138(11)	0.0125(8)	0.0117(8)	0.0125(8)	0.0117(6)	0.0103(9)	0.0109(11)	0.0152(12)	0.0145(13)	0.0092(17)
O3											
x	0.3516(2)	0.3522(6)	0.3533(5)	0.3540(4)	0.3553(5)	0.3559(4)	0.3562(5)	0.3553(6)	0.3576(6)	0.3565(7)	0.3576(8)
y	0.0183(2)	0.0198(7)	0.0214(6)	0.0224(6)	0.0235(7)	0.0227(5)	0.0254(7)	0.0263(7)	0.0281(6)	0.0283(8)	0.0309(10)
z	0.9952(3)	0.9938(6)	0.9906(6)	0.9877(5)	0.9872(5)	0.9859(4)	0.9854(7)	0.9838(9)	0.9846(8)	0.9847(9)	0.9867(10)
Uiso	0.0101(3)	0.0101(9)	0.0106(7)	0.0106(7)	0.0085(7)	0.0090(6)	0.0094(8)	0.0083(11)	0.0087(11)	0.0095(11)	0.0048(14)

Table 4 Selected bond lengths (Å) and angles (°), polyhedral volume (Å³) and distortion parameters of augite at ambient and high pressures to 26.65 GPa. Note: Nomenclature after Zhang et al., (1997).

(a) $M2O_8$ polyhedron

Pressure (GPa)	0.0001	1.05(5)	3.65(7)	6.55(4)	8.30(4)	11.40(3)	14.25(2)	17.55(1)	20.35(2)	23.85(1)	26.65(2)
M2-O1(A1, B1)	2.341(2)	2.336(4)	2.327(6)	2.312(6)	2.297(6)	2.288(5)	2.279(6)	2.241(7)	2.242(7)	2.222(9)	2.222(7)
M2-O2(C2, D2)	2.362(2)	2.347(6)	2.332(4)	2.321(3)	2.311(4)	2.302(3)	2.297(3)	2.275(4)	2.268(4)	2.270(5)	2.262(5)
M2-O3(C1, D1)	2.552(2)	2.549(6)	2.540(5)	2.526(5)	2.514(6)	2.487(4)	2.476(6)	2.470(7)	2.454(7)	2.439(8)	2.427(7)
M2-O3(C2, D2)	2.709(2)	2.680(6)	2.626(5)	2.578(5)	2.545(5)	2.518(4)	2.478(5)	2.451(6)	2.414(6)	2.401(7)	2.370(7)
Mean bond length	2.4909	2.4779	2.4564	2.4342	2.4169	2.3988	2.3825	2.3595	2.3446	2.3328	2.3203
Volume	25.5418	25.2239	24.6351	23.9899	23.5001	22.9983	22.6351	22.0410	21.6447	21.3856	21.0754
Distortion index	0.05605	0.05503	0.05158	0.04835	0.04658	0.04317	0.03964	0.04286	0.03814	0.03725	0.03362

(b) $M1O_6$ octahedron

Pressure (GPa)	0.0001	1.05(5)	3.65(7)	6.55(4)	8.30(4)	11.40(3)	14.25(2)	17.55(1)	20.35(2)	23.85(1)	26.65(2)
M1-O1(A1, B1)	2.114(2)	2.099(7)	2.087(6)	2.059(6)	2.042(6)	2.014(5)	2.010(6)	1.994(8)	1.973(4)	1.960(5)	1.948(5)
M1-O1(A2, B2)	2.045(2)	2.047(3)	2.033(3)	2.018(3)	2.011(3)	2.000(2)	1.993(3)	1.984(4)	1.983(7)	1.965(9)	1.948(8)
M1-O2(C1, D1)	2.029(2)	2.035(8)	2.020(6)	1.997(6)	1.991(7)	1.980(6)	1.976(6)	1.966(8)	1.957(8)	1.931(8)	1.875(8)
Mean bond length	2.0627	2.0604	2.0469	2.0246	2.0147	1.9978	1.9931	1.9813	1.9709	1.9520	1.9239
Volume	11.6003	11.5679	11.3341	10.9632	10.7989	10.5231	10.4555	10.2593	10.0957	9.7793	9.3356
Distortion index	0.01649	0.01248	0.01317	0.01126	0.00907	0.00598	0.00571	0.00524	0.00473	0.00716	0.01696
Quadratic elongation λ	1.0062	1.0056	1.0061	1.0063	1.0066	1.0070	1.0065	1.0075	1.0074	1.0094	1.0117
Bond angle variance σ^2	19.6504	18.5428	19.9639	20.9821	21.9413	23.3730	22.2517	25.7723	25.4550	32.2050	39.1661

(c) TO_4 tetrahedron

Pressure (GPa)	0.0001	1.05(5)	3.65(7)	6.55(4)	8.30(4)	11.40(3)	14.25(2)	17.55(1)	20.35(2)	23.85(1)	26.65(2)
T-O1(C1)	1.612(2)	1.609(5)	1.604(5)	1.600(4)	1.603(5)	1.598(3)	1.581(5)	1.587(7)	1.574(6)	1.570(8)	1.594(9)
T-O2(C1)	1.595(2)	1.572(8)	1.577(6)	1.583(6)	1.585(7)	1.586(6)	1.556(6)	1.560(7)	1.554(8)	1.566(9)	1.586(8)
T-O3(C1)	1.667(1)	1.667(5)	1.665(4)	1.661(4)	1.663(4)	1.661(3)	1.653(4)	1.645(5)	1.647(5)	1.638(6)	1.621(6)
T-O3(C2)	1.688(2)	1.695(5)	1.685(5)	1.674(4)	1.677(5)	1.664(4)	1.666(5)	1.651(6)	1.667(6)	1.660(7)	1.671(7)
Mean bond length	1.6403	1.6359	1.6327	1.6297	1.6321	1.6273	1.6142	1.6107	1.6103	1.6085	1.6180
Volume	2.2457	2.2253	2.2155	2.2027	2.2113	2.1904	2.1384	2.1261	2.1212	2.1145	2.1532
Distortion index	0.02248	0.02779	0.02582	0.02331	0.02326	0.02165	0.02826	0.02314	0.02873	0.02516	0.01711
Quadratic elongation λ	1.0062	1.0074	1.0062	1.0062	1.0065	1.0070	1.0071	1.0064	1.0077	1.0074	1.0068
Bond angle variance σ^2	26.4038	30.2510	25.6264	26.1053	27.2935	28.7848	28.8200	25.9136	31.4456	30.9482	28.9754

O3-O3-O3	166.0(1)	164.9(3)	163.6(3)	162.9(3)	162.1(4)	162.7(3)	160.8(4)	160.2(4)	158.9(4)	158.8(4)	157.0(4)
----------	----------	----------	----------	----------	----------	----------	----------	----------	----------	----------	----------

Table 5 Linear BM3 fitting parameters and axial compressibilities of the lattice parameters a , b and c

	a	b	c
$M_0(\text{GPa})$	362(24)	250(12)	327(6)
M'	18(4)	9(1)	16(1)
$\beta_0(\text{GPa}^{-1})$	0.0028(2)	0.0040(2)	0.00306(6)

Table 6 Eulerian Strain tensor at different pressures

Pressure (GPa)	Eulerian finite strain along each major axis (Negative values indicate compression)			Directions of the major axes represented by their angles with <i>a</i> -, <i>b</i> - and <i>c</i> -axes of the unit cell lattice								
	“Soft” axis in <i>a-c</i> plane(ϵ_1)	<i>b</i> -axis(ϵ_2)	“Hard” axis in <i>a-c</i> plane(ϵ_3)	“Soft” axis in <i>a-c</i> plane(ϵ_1)			<i>b</i> -axis(ϵ_2)			“Hard” axis in <i>a-c</i> plane(ϵ_3)		
0.0001	-0.0029(2)	-0.0081(5)	0.0009(3)	58.5(0.0)	90.0(0.0)	164.5(0.0)	90.0(0.0)	0.0(0.0)	90.0(0.0)	148.5(0.0)	90.0(0.0)	105.5(0.0)
1.05(5)	-0.0122(2)	-0.0151(5)	-0.0033(3)	45.3(0.0)	90.0(0.0)	150.9(0.0)	90.0(0.0)	0.0(0.0)	90.0(0.0)	135.3(0.0)	90.0(0.0)	119.1(0.0)
3.65(7)	-0.0216(2)	-0.0238(5)	-0.0080(3)	42.4(0.0)	90.0(0.0)	147.8(0.0)	90.0(0.0)	0.0(0.0)	90.0(0.0)	132.4(0.0)	90.0(0.0)	122.2(0.0)
6.55(4)	-0.0265(2)	-0.0274(5)	-0.0106(3)	40.7(0.0)	90.0(0.0)	145.9(0.0)	90.0(0.0)	0.0(0.0)	90.0(0.0)	130.7(0.0)	90.0(0.0)	124.1(0.0)
8.30(4)	-0.0337(2)	-0.0367(5)	-0.0145(3)	41.8(0.0)	90.0(0.0)	146.8(0.0)	90.0(0.0)	0.0(0.0)	90.0(0.0)	131.8(0.0)	90.0(0.0)	123.2(0.0)
11.40(3)	-0.0399(2)	-0.0461(5)	-0.0181(3)	42.7(0.0)	90.0(0.0)	147.6(0.0)	90.0(0.0)	0.0(0.0)	90.0(0.0)	132.7(0.0)	90.0(0.0)	122.4(0.0)
14.25(2)	-0.0462(2)	-0.0556(5)	-0.0213(3)	43.0(0.0)	90.0(0.0)	147.8(0.0)	90.0(0.0)	0.0(0.0)	90.0(0.0)	133.0(0.0)	90.0(0.0)	122.2(0.0)
17.55(1)	-0.0511(2)	-0.0609(5)	-0.0247(3)	42.2(0.0)	90.0(0.0)	146.8(0.0)	90.0(0.0)	0.0(0.0)	90.0(0.0)	132.2(0.0)	90.0(0.0)	123.2(0.0)
20.35(2)	-0.0569(2)	-0.0694(5)	-0.0283(3)	43.6(0.0)	90.0(0.0)	148.2(0.0)	90.0(0.0)	0.0(0.0)	90.0(0.0)	133.6(0.0)	90.0(0.0)	121.8(0.0)
23.85(1)	-0.0619(2)	-0.0760(5)	-0.0313(3)	44.4(0.0)	90.0(0.0)	148.8(0.0)	90.0(0.0)	0.0(0.0)	90.0(0.0)	134.4(0.0)	90.0(0.0)	121.2(0.0)

Table 7 Thermoelastic properties of high pressure minerals used for density calculations.

Mineral	V_0 (\AA^3)	K_{T0} (GPa)	K_{T0}'	$\partial K_0/\partial T$	$\alpha_0 \times 10^{-5}$	$\alpha_1 \times 10^{-8}$ (K^{-1})
Jadeite ^a	403.32(8)	124.5(4.0)	5.0(fixed)	-0.016(5)	2.56(22)	0.26(18)
Aegirine ^b	431.5(1)	118(3)	4.2(3)	-0.016(5)	2.64(13)	0
Diopside ^c	438.67(6)	109(4)	4.8(6)	-0.021(4)	2.32(5)	1.88(7)
Omphacite ^d	424.7(7)	126(1)	4.0(fixed)	-0.015(4)	2.2(1)	0
Clinoenstatite ^e	405.0(2.6)	106.9(25.9)	5.3(3.9)	-0.021(10)	2.01(44)	2.1(1.1)

References: a-Zhao et al. (1997); b-Tribaudino et al. (2008) and Xu et al. (2016), note that $\partial K_0/\partial T$ was assumed to be the same as in jadeite (no data of $\partial K_0/\partial T$ for aegirine is currently available); c-Zhao et al. (1998); d-Nishihara et al. (2003); e-Shinmei et al. (1999)